

ABSTRACT

ADAMS IV, WILLIAM TAYLOR. Gallium Based Oxide Interfaces (Under the direction of Dr. Albena Ivanisevic).

The main topic of this thesis is a discussion of nanostructured gallium oxyhydroxide particles and their interfacial properties in a variety of environments. The surface chemistry of gallium oxide and gallium oxyhydroxide materials is largely unexplored, and their high band gap gives rise to many interesting applications. The 4.7 - 4.8 eV band gap is high enough for UV photoluminescence and electron holes created by UV excitation have sufficient oxidation potential to break C-C bonds. These effects alone make interesting applications possible in catalysis, radiosensitization, and bio-therapeutics. Nanoparticle anisotropy was explored via in vitro experiments to test the radiosensitization effect of different nanoparticle morphologies and interfaces under X-ray irradiation. Most of the subsequent work involved functionalization of GaOOH nanostructures with reactive dyes RR198, RB19, RB49 and RY174 with functional groups containing sulfonic, phosphonic or carboxylic acid functionalities that can interact with the native GaOOH surface through dangling -OH bonds or through chemi/physisorption. The extent of the effect of functionalization can vary with route of ligand attachment with in-situ reaction protocol resulting in the greatest nanoparticle morphological changes. Mixed Al/Ga Oxide hydroxides in conjunction with in-situ and ex-situ reactive dye functionalization protocol were explored in an effort to make layered nanostructures with unique optical properties. Further experiments with Reactive Red 198 and Fluorescein Sodium salt explored the relative affinity of sulfonic and carboxylic acid groups for the GaOOH nanoparticle surface.

© Copyright 2020 by William Taylor Adams IV

All Rights Reserved

Gallium Based Oxide Interfaces

By
William Taylor Adams IV

A dissertation submitted to the Graduate Faculty of
North Carolina State University
in partial fulfillment of the
requirements for the degree of
Doctor of Philosophy

Materials Science and Engineering

Raleigh, North Carolina
2020

APPROVED BY:

Dr. Albena Ivanisevic
Committee Chair

Dr. Tania Paskova

Dr. Lewis Reynolds Jr.

Dr. Nelson Vinueza Benitez

BIOGRAPHY

W. Taylor Adams IV did his undergraduate at Clemson University as a major in Inorganic Materials Science and Engineering. He worked with Albena Ivanisevic on morphological modification of nanostructured gallium oxyhydroxide and their surface functionalization at North Carolina State University after being accepted in the PhD program for Materials Science and Engineering in 2016.

ACKNOWLEDGMENTS

I would like to thank my supervisor, Dr. Albena Ivanisevic for pushing me to be my best and for her guidance through this process. I would also like to thank my family for their continual support, without them I would not have made it this far.

TABLE OF CONTENTS

Chapter 1: Nanostructured Oxides Containing Ga: Materials with Unique Properties for Aqueous Based Applications	1
1.1 Introduction.....	1
1.2 Synthesis of Ga containing Oxides	3
1.3 Chemical Functionalization of Ga Containing Oxides in Aqueous Solutions	5
1.4 Applied Interfaces based on Ga Containing Oxides in Aqueous solutions	7
1.5 Conclusions and outlook.....	9
Chapter 2: Ga-Ion Enhanced and Particle Shape Dependent Generation of Reaction Oxygen Species in X-Ray Irradiated Composites	14
2.1 Introduction.....	14
2.2 Results and Discussion	17
2.3 Conclusions.....	23
2.4 Experimental Section	24
Chapter 3: Nanostructured GaOOH modified with reactive yellow, red and blue water-soluble dyes	30
3.1 Introduction.....	30
3.2 Synthesis	31
3.3 Discussion.....	32
3.4 Conclusion	37
Chapter 4: Synthesis of Mixed Ga Based Oxides in the Presence of Water-Soluble Adsorbates	42
4.1 Introduction.....	42
4.2 Experimental.....	43
4.3 Results and Discussion	44
4.4 Conclusions.....	49
Chapter 5: Exchange Reactions on GaOOH nanostructured surface	52
5.1 Introduction.....	52
5.2 Experimental.....	53
5.3 Discussion.....	55
5.4 Conclusions.....	62
Chapter 6: Conclusions and Future Outlook	67
References	70

LIST OF TABLES

Table 1.1	Summary of representative methods used to fabricate Ga containing oxides.....	10
Table 1.2	Summary of representative sizes and shapes of reported Ga containing oxides along with methods for their characterization.....	11
Table 2.1	Summary of differences in the amount of Ga leached compared to the initial value on day 0 immediately after placing the particles in solution.....	23
Table 3.1	Summary of SEM Analysis of the Synthesized Materials	40
Table 3.2	Summary of the Deconvoluted C 1s XPS Data.....	41
Table 3.3	Summary of the Deconvoluted O 1s XPS Data	41
Table 5.1	Comparison of qualitative changes of each species with respect to clean GaOOH nanoparticles	63

LIST OF FIGURES

Figure 1.1	Possible binding modes of thiol (1), carboxylic acid (2), and phosphonic acid adsorbates (3 – monodentate; 4, 6 – bidentate; 5- tridentate) to surfaces terminated on Ga containing oxides.....	12
Figure 1.2	Recent applied studies with Ga containing oxides: A) Mesoporous Ga ₂ O ₃ -TiO ₂ nanocomposite for efficient photodecomposition of herbicide imazapyr (copyright 2018 Elsevier); B) Fabrication and testing of Ga ₂ O ₃ anode for lithium-ion batteries (copyright 2018 American Chemical Society); C) Persistent luminous nanoparticles (PLNPs) containing Ga oxides that can be used in cancer theranostic applications after chemical functionalization (copyright 2018 American Chemical Society).....	13
Figure 2.1	Representation of the approach used to test the role of shape of GaOOH particles on PC12 cell viability and ROS production.	26
Figure 2.2	Representative SEM images of the different shapes of GaOOH used in the study: A) anisotropic and B) orzo. Parts C) and D) show zoomed in structures for the anisotropic and orzo shapes, respectively.	27
Figure 2.3	XRD characterization of the different Ga containing materials used in the study: a) anisotropic GaOOH particles and b) orzo GaOOH particles	27
Figure 2.4	Cell viability assay results in the absence of GaOOH material: a) AB assay conducted in the presence of no material, just Matrigel; b) AB assay conducted in the presence of no material and after the indicated radiation treatment.....	28
Figure 2.5	Summary of the cell viability assays performed with Alamar Blue after the indicated times in days, exposure to different amount of radiation and in the presence of the specified concentrations of a) nitrate salt; b) anisotropic GaOOH; and c) orzo GaOOH.....	28
Figure 2.6	Summary of the ROS assays performed with DCFH-DA after the indicated times in days, exposure to different amount of radiation and in the presence of the specified concentrations of a) nitrate salt; b) nitrate salt and PC12 cells seeded on top of the Ga containing composite; c) anisotropic GaOOH; d) anisotropic GaOOH and PC12 cells seeded on top of the Ga containing composite; e) orzo GaOOH; f) orzo GaOOH and PC12 cells seeded on top of the Ga containing composite.....	29
Figure 3.1	Chemical structures of the four different dyes.	38
Figure 3.2	GaOOH particles at A) 60kx magnification B) 100kx magnification.....	38
Figure 3.3	Comparison among elemental compositional changes extracted from XPS data	39

Figure 4.1	Summary of representative SEM data for each composition synthesized	50
Figure 4.2	Summary of the XRD characterization performed on all of the particle compositions synthesized in this work	50
Figure 4.3	FT-IR data of the dried nanoparticles samples synthesized with different precursors and variable in situ (In) and ex-situ (Ex) conditions	51
Figure 4.4	Comparison among all the PL signatures for the synthesized materials	51
Figure 5.1	Structure of dyes used to functionalize GaOOH nanoparticles	63
Figure 5.2	A) C 1s spectra for clean GaOOH B) O 1s XPS spectra for clean GaOOH, C) C 1s XPS spectra for FSS dye reference D) O 1s XPS spectra for FSS dye reference E) C 1s XPS spectra for RR198 dye reference F) O 1s XPS spectra for RR198 dye reference	64
Figure 5.3	A) C 1s XPS spectra for RR198 functionalized GaOOH nanoparticles, B) O 1s XPS spectra for RR198 functionalized GaOOH nanoparticles, C) C 1s XPS spectra for FSS functionalized GaOOH nanoparticles, D) O 1s XPS spectra for FSS functionalized GaOOH nanoparticles	65
Figure 5.4	A) C 1s XPS spectra for RR198:FSS functionalized GaOOH nanoparticles, B) O 1s XPS spectra for RR198:FSS functionalized GaOOH nanoparticles, C) C 1s XPS spectra for FSS:RR198 functionalized GaOOH nanoparticles, D) O 1s XPS spectra for FSS:RR198 functionalized GaOOH nanoparticles	66

CHAPTER 1

Nanostructured Oxides Containing Ga: Materials with Unique Properties for Aqueous Based Applications

1.1 Introduction

Prior to this decade Ga containing materials have been predominantly used in micro-electronics. For instance, the optoelectronics community is currently addressing the need to produce single crystal Ga_2O_3 with specific characteristics (i.e. p-type doping and improved thermal conductivity) that are essential for fabricating devices for power electronics.¹ However, advances in the synthesis of nanostructured Ga based oxide materials has expanded their utility.^{2,3} Currently there is an emphasis on understanding their properties in the context of catalysis,⁴ sensors,⁵ and biomedical modalities⁶ such as targeted drug delivery, chemo/thermal/photodynamic therapy and *in vivo* imaging. Properties of particular interest include unique conductivity⁷ and photoluminescence.⁸ Additionally, these nanostructured oxides are often incorporated into specific processing where cost-effective, large scale production is essential along with chemical and thermal stability over broad ranges and conditions,⁹ as well as high transparency and tunable luminescence.

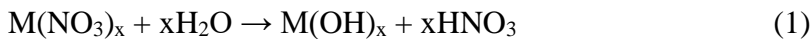
The potential applications of these materials have prompted a number of efforts to improve the materials' synthesis using several general routes, Table 1.1. Ga based oxides have been primarily studied in two forms: Ga_2O_3 and GaOOH . Recent work has focused on controlling their size, aspect ratio as well as processing-based parameters such as the use or elimination of surfactant during synthesis in solution. The prospective will focus on the challenges and opportunities associated with not only making these materials but also further modifying them via chemical

functionalization.¹⁰ Additional surface chemistry on Ga₂O₃ and GaOOH can improve their stability in aqueous solutions.¹¹ However, surface passivation is not the only motivation for the development of surface chemistry routes to alter them. Additional optical properties that can change include photoluminescence¹² and persistent photoluminescence.¹³

There are unique materials chemistry aspects that one needs to consider in tailoring the properties of Ga₂O₃ and GaOOH in aqueous based applications. For example, as synthesized Ga₂O₃ and GaOOH are negatively charged and their surface can readily be coronated by proteins when introduced into the conditions associated with *in vitro* or *in vivo* studies. Furthermore, already modified Ga₂O₃ and GaOOH nanostructured particles can experience dissociation of weakly bound ligands in aqueous solutions under different temperatures and pHs. This dissociation can lead to agglomeration, alter desired properties and lead to irreproducibility during processing procedures. Combined computational and experimental studies have highlighted the importance of surface structure and reactivity of the oxide surface with respect to stability of specific ligand attachment in water.¹⁴ This prospective will appeal to a wide audience due to the emerging use in Ga₂O₃ and GaOOH in many fields where low inorganic materials' toxicity and preparation in environmentally friendly solvents such as water is desired. We summarize current efforts to improve the utility of Ga containing oxides in aqueous solutions in order to achieve desired stability, as well as optical characteristics that are needed in areas ranging from environmental monitoring in extremely harsh environments to solution-based biochemical sensors.

1.2 Synthesis of Ga containing oxides

Table 1.1 summarizes representative examples of Ga containing oxides that have been reported in the literature. In several instances these oxides are subsequently converted to other products (i.e. GaN, B-Ga₂O₃ or A-Ga₂O₃). A few of the synthesis methods offer specific advantages when adapting Ga containing oxides for aqueous based applications. A number of reports describe solution-based techniques resulting in Ga containing nanostructured materials. Examples include microemulsion, sol-gel, hydrothermal and ultrasonic assisted fabrication. Furthermore, researchers have performed the hydrothermal synthesis under microwave radiation in an effort to improve final yield while reducing reaction times. Column 2 of Table 1.1 identifies metal nitrate salts as one of the more commonly used precursors to make these materials. The formation of the final materials proceeds in two steps where a hydrolysis of the salt results in the formation of a metal hydroxide. Subsequently the hydroxide is dehydrated, a precipitate is observed and further drying yields the metal oxide. The two reactions are summarized as described by Hayashi et al.¹⁵



Surfactant molecules have also been utilized during the synthesis of these materials. During this process the surfactant is used together with a stabilizer often referred to as an emulsifier. The molecule chosen as a stabilizer has a polar head group and nonpolar tail. During the synthesis of the Ga containing oxides, the surfactant and emulsifier are mixed together with the metal salt precursors. As the mixture is formed the emulsifier is using its nonpolar tail to face towards the

surfactant while its polar head group orients towards the aqueous solution containing the precursor materials. During this process the size and shape of the Ga containing oxide is controlled by the emulsifier which is around the reaction solution where the product crystallizes.

Another methodology used to control the size of Ga containing particles is via a sol-gel where a polymerization reaction takes place. The chosen precursor materials identified in Table 1.1 form gels through a hydrolysis reaction. One can tune the size of the particles by controlling the rate of the hydrolysis reaction in addition to any condensation that might take place. A drawback of this methodology is the need to remove solvents by calcination which requires elevated temperatures. A methodology that does not require any additional heat or pressure is the sonochemical route where chemical reactions are initiated by ultrasonic radiation. The use of ultrasound promotes the formation of bubbles in the solution which continue to grow until they collapse. These bubbles are thought to produce extremely high temperatures during the process of their collapse which are then rapidly cooled back to the ambient solution temperature. By far the most widely used route to make Ga containing oxides in a number of papers is the traditional hydrothermal synthesis techniques where a solution of precursors is sealed and placed into an autoclave. The reaction can take up to 24 hours. However, if one replaces the autoclave with a microwave, these reactions can be done in less than an hour. Additional advantages include the elimination of need for a surfactant and the use of deionized water as a solvent. Literature sources cite the reduced reaction time as the key advantage of the microwave synthesis.

Many of the summarized synthetic methods have focused on controlling shape and size. Table 1.2 lists the ranges of sizes and examples of shapes reported in the literature. The use of general terms such as 'base' or 'weak base' are intended to denote that a wide range of chemicals can be used to perform the synthesis. The Ga containing oxide particles dimensions and

geometrical variations have been linked to specific properties quantified by a wealth of analytical techniques listed in the last column of the table. In addition to control the over surface to volume ratios, size and shape have been linked to a number of anisotropy dependent properties. Ga containing oxides can adapt different shapes during the different synthesis steps and show shape dependent stability in aqueous solutions. Differences in stability are particularly noteworthy in complex biological solutions where release of Ga ions can lead to variable physiological responses of cells.¹⁶ In addition to stability, the thermal, spectral, and photocatalytic properties of Ga containing nanostructure are also size and shape dependent.¹⁷ β -Ga₂O₃ nanobelts obtained via mechanical exfoliation under room temperature and humidity conditions have been incorporated into devices that show remarkable radiation tolerance.¹⁸ Many of the spectroscopic studies summarized in Table 1.2 have examined the role of water hydrogen bonded to the Ga₂O₃ and GaOOH nanostructured materials. Infrared bands associated with bonding to hydroxyl units are reported to be sensitive to synthesis conditions.¹⁹ Additional spectroscopic studies have concluded that the luminescence of these materials is nanocrystalline size dependent and the location of the emission peak is in the blue-green region.²⁰ The intensity and the broadness of the emission peak of Ga containing oxides is not altered in aqueous solutions, and its after-glow or persistent luminescent properties are showing promise in pre-clinical *in vitro* and *in vivo* imaging studies.²¹

1.3 Chemical functionalization of Ga containing oxides in aqueous solutions

Chemical functionalization not only improves the stability of Ga containing oxides in aqueous solutions but can also add to their functionality by tailoring properties such as emission and chemical recognition.²² Certain surface planes have been shown to be more stable than others as is the case for β -Ga₂O₃ (100)-B which can lead to difficulties in the development of successful functionalization routes.¹⁴ In many instances, the hydroxide groups present on the surface have

proven effective moieties for the covalent modification of the surface with a number of moieties. Typical adsorbates considered in the literature include thiols, alcohols, carboxylic acid, and phosphonic acid derivatives. Some of these adsorbates can engage in various modes of binding to the Ga oxide containing surface, Figure 1. The desired chemisorption can be accomplished *ex-situ* by taking the already made nanostructured Ga containing oxide and exposing it to the chosen adsorbate.²³ Procedures can focus on tuning incubation times, temperature and ligand concentration. The mode of binding of each type of adsorbate is dependent on what type of surface structure is energetically more favorable, though experimental results report observations of multiple modes of binding with specific ligands.²⁴

With respect to functionalization recent work has focused on a different approach to modify the nanostructured Ga containing oxides. The so-called *in-situ* procedure modifies the material during the synthesis. Several advantages are cited including ease of preparation, shorter time needed to prepare the final product and use of water as a solvent when the Ga salt precursor is mixed with a solution containing water soluble adsorbates with functional groups that have an affinity for the oxide. During the *in-situ* protocol it is important to consider the Pourbaix diagram for Ga.²⁵ This element is passivated in small pH windows and during the *in-situ* procedure varying pH values can result in leaching of Ga.

During the *in-situ* procedure as the Ga₂O₃ or GaOOH is formed the inherent presence of oxides eliminates the need for an etchant which is required for the *in-situ* modification of other Ga containing materials such as GaN.²⁶ This process represents a highly scalable and environmentally friendly technique for forming organic/inorganic hybrids with long term interface stability. Representative literature reports have used cyclodextrin,²⁷ phosphonic acid²² and carboxylic acid²⁸ derivatives for *in-situ* functionalization of Ga-containing oxides. In the cases of phosphonic acid

derivatives the passivation achieved via the *in-situ* procedure resulted in exceptional ligand stability compared to passivation done *ex-situ*.²² Water soluble dye molecules with carboxylic acid moieties have been also utilized to modify GaOOH *in-situ* and *ex-situ*. In contrast to other organic acid derivatives the ones containing carboxylic acids showed excellent stability in water regardless of what method was used for their preparation.²⁸ These results support the notion that carboxylic acid derivatives have greater affinity for Ga containing oxides surfaces compared to other ligands with other functional groups.

It is important to note in the context of *in-situ* functionalization of Ga containing oxides the recent interest in understanding of how to control the complex oxides that include gallium when nanostructured materials are formed from liquid metals.²⁹ Representative ligands used to control the synthesis of these materials and to modify the nanostructured Ga containing oxide shell of these materials include: thiols, cetrimonium bromide, poly(4-vinyl-1-methyl-pyridinium bromide), lysozyme, oleic acid, and dodecylamine.^{30,31,32} Not all studies have focused on understanding the nature of the bonding between the oxide and the chosen ligand, but they have all demonstrated that the ligands do control the desired shape and size.

1.4 Applied interfaces based on Ga containing oxides in aqueous solutions

We highlight three recent examples published in the last 20 months of incorporating Ga containing oxides in interfaces that benefit from preparation or use in aqueous solutions. The chosen examples are representative of the unique properties associated with the oxides. We have specifically chosen examples that derive the materials through methods other than liquid metal approaches because these have been the subject of other recent extensive reviews in the literature.

The synthesis of metal oxides is often motivated by their potential to perform better in photocatalytic applications. Ismael et al. have prepared mesoporous Ga₂O₃-TiO₂ nanocomposites

and have demonstrated its efficient photodecomposition of a herbicide.³³ The method used to make the Ga containing oxide is based on the sol-gel in the presence of copolymer. The amount of Ga₂O₃ was tuned during the synthesis by controlling the starting amount of Ga salt used. The unique structure and composition of the composite contributed to its mechanism of action, Figure 1.2A. Specifically, the increased amounts of defects associated with a large content of Ga₂O₃ is attributed to superior ability to trap holes and prevent recombination. The authors concluded that the improved photocatalytic performance can be traced to the greater number of acceptor states with respect to Ga₂O₃ present in the amorphous phase. This conclusion was supported by luminescence measurements. Additional attributes of the Ga containing oxide composite are fabrication reproducibility and stability of the water, as well as the fact that it can be recycled in multiple cycle while maintaining high efficiency.

Nanostructured Ga containing oxides have recently shown promise in lithium-ion batteries. The methodology is depicted in Figure 1.2B.³⁴ We summarize key features associated with the use of Ga oxides in this example. The particles are prepared via a hydrothermal carbonization method that controls their size to 2.6 nm and ensures the formation of a carbon shell around each particle. The key feature is that during the lithiation process the carbon shell prevents the particles from aggregation. Because lithium-ion batteries are intended to be re-chargeable, stability and lack of aggregates is key during the cycling evaluation of anode and cathode materials. The reported Ga₂O₃ based anode showed superior characteristics due to its ability to prevent the formation of surface aggregates while still forming Ga⁰ during the lithiation process.

In biomedical applications ability to control the optical properties of nanostructured materials is valuable in designing imaging and targeting applications. Nanostructured Ga containing oxides show particularly noteworthy promise for these applications due to their

persistent luminescence properties. A recent advance in particle design showed that nanostructured particles with hollow cavities that are decorated with Ga oxides show an afterglow effect due to their persistent photoluminescence, Figure 1.2C.²¹ These Ga oxide-containing particles are amenable to other aqueous solution processing that can enhance their chemo and photodynamic attributes, in addition to the promise they show in imaging. Most importantly for these types of applications the particle stability was verified *in vitro* and *in vivo*. This observation along with ability to accommodate higher drug loading renders the material very promising for multi-modality biomedical procedures.

1.5 Conclusions and Outlook

Variety of methods exist to synthesize Ga containing oxides and many methods have developed reliable strategies to control the size and the shape of these materials. Because of their favorable properties with respect to robustness in different environments, tunability of excitation and emission properties, and photoconductivity a number of efforts have demonstrated the promise of the material in applications that include a wide range spanning the energy and catalysis fields and extending all the way to pre-clinical biomedical studies. There are many opportunities that still exist with respect to fundamental materials chemistry and surface chemistry research on Ga containing oxides. There is a need to increase the number of variable geometries associated with these materials as well as compositional mixtures with other elements. These types of materials have the potential to exhibit interesting plasmonic properties. Further research is needed to elucidate the surface bonding modes with different adsorbates and develop methods to control the adsorption of ligands on Ga containing oxides. A relatively unexplored surface chemistry on these materials exists with respect to utilization of ligand exchange reactions as well as the usage of

ligands with variable functional groups. Taken together current and future advances in the field of Ga containing oxides are projected to increase their potential for practical applications.

Table 1.1 Summary of representative methods used to fabricate Ga containing oxides.

<i>Product</i>	<i>Precursors</i>	<i>Processing Technique</i>	<i>References</i>
<i>Mixed oxyhydroxide</i>	Metal nitrates, weak base	Sol gel / hydrothermal	12,35,36
<i>Ga₂O₃:MO₂</i>	Metal nitrates, Si(OC ₂ H ₅) ₄ , Ti(OC ₂ H ₅) ₄	Sol gel	37,33
<i>Dy:β-Ga₂O₃</i>	Dy ₂ O ₃ , β-Ga ₂ O ₃ , citric acid (C ₆ H ₈ O ₇), polyethylene glycol	Sol gel 75°C	38
<i>β-Ga₂O₃</i>	β-Ga ₂ O ₃	Single crystal growth	39
<i>β-Ga₂O₃</i>	GaAs, N ion, air (Oxygen)	Ion implantation	40,41
<i>β-Ga₂O₃</i>	GaCl ₃ , NaOH	Combustion synthesis	20,42,43,44,45,46
<i>β-Ga₂O₃</i>	Ga metal, (patterned p-Si substrate), (Au NP)	Chemical Vapor Deposition	47,48,3,5,49,50,51
<i>γ-Ga₂O₃</i>	Ga Salt, base	Hydrothermal → Calcination	52,8
<i>β-Ga₂O₃</i>	Ga Salt, base, organic template	Wet chemistry (template optional)	53,54,55,27
<i>Eutectic-GaIn, Ga</i>	Ga, In, Organic stabilizing ligand (thiol, phenol)	Liquid metal ultrasonication	30,56,32
<i>Eutectic-GaIn</i>	In, Ga	High temperature oxidation	29
<i>Gd-Al-Ga₂O₃</i>	Gd ₂ O ₃ , Ga ₂ O ₃ , (NH ₄)Al(SO ₄) ₂ , HNO ₃ , NH ₃ , NH ₄ HCO ₃	Co-precipitation	57
<i>GaON</i>	Ga(NO ₃) ₃ , (CH ₂) ₆ N ₄	Hydrothermal	9
<i>GaOOH</i>	Ga metal	Laser ablation	58
<i>GaOOH</i>	GaCl ₃	Sonochemical	59
<i>GaOOH</i>	GaN	Ball mill	60
<i>GaOOH</i>	Ga(NO ₃) ₃ (NaOH)	Hydrothermal	16,61,62,63,64,2
<i>GaOOH</i>	Ga metal	Ultrasonication	4
<i>GaZnON</i>	Ga ₂ O ₃ , ZnO, HCl, NaOH, Na ₂ CO ₃	Hydrothermal	65
<i>In/Ga/InGa oxide</i>	In, Ga, lysozyme	Hydrothermal with surfactant	31
<i>LaGaO₃</i>	La, Ga, C ₅ H ₇ O ₂ -	Chemical vapor synthesis	66
<i>Nd:Gd-Ga₂O₃</i>	Ga ₂ O ₃ , Gd ₂ O ₃ , Nd ₂ O ₃	Microwave combustion of gel	67

Table 1.2 Summary of representative sizes and shapes of reported Ga containing oxides along with methods for their characterization

<i>Ga containing oxide</i>	<i>Shape</i>	<i>Size</i>	<i>Analytical Characterization</i>	<i>Ref.</i>
β -Ga ₂ O ₃ or β -Ga ₂ O ₃ :MyOx	Sphere	2-15 nm	A, B, D, E, F, N, P, R, T, U, †, ‡	37,32
β -Ga ₂ O ₃ or β -Ga ₂ O ₃ :MyOx	Sphere	15-80 nm	A, B, D, E, F, P, R, S, T	43,35
β -Ga ₂ O ₃ or β -Ga ₂ O ₃ :MyOx	Sphere	100-200 nm	D, F, N, P, R, S, T, U, †, ‡	55
β -Ga ₂ O ₃ or β -Ga ₂ O ₃ :MyOx	Rice/Orzo	200 nm -1 μ m length	D, F, I, S, T	68
β -Ga ₂ O ₃ or β -Ga ₂ O ₃ :MyOx	Rice/Orzo	1-4 μ m	D, E, F, P, S, U, †, ‡, †	54
β -Ga ₂ O ₃ or β -Ga ₂ O ₃ :MyOx	Rod	80x30 nm length x width	D, †, †	69
β -Ga ₂ O ₃ or β -Ga ₂ O ₃ :MyOx	Rod	200-1000 nm * 50-100 nm	D, P, R, U, †, ‡	70
β -Ga ₂ O ₃ or β -Ga ₂ O ₃ :MyOx	Rod	1-4 μ m x 100-500 nm	D, E, F, N, P, R, S, U, †, ‡, †	54
β -Ga ₂ O ₃ or β -Ga ₂ O ₃ :MyOx	Wire/needle	30-100 nm diameter	D, P, R, S, †, ‡	47
β -Ga ₂ O ₃ or β -Ga ₂ O ₃ :MyOx	Wire/needle	200-500 nm diameter	D, I, L, P, S	5
β -Ga ₂ O ₃ or β -Ga ₂ O ₃ :MyOx	Knotted Chain	knots 400nm, spindle 50nm	D, E, S, T, ‡	49
β -Ga ₂ O ₃ or β -Ga ₂ O ₃ :MyOx	Ribbon	1-3 μ m wide	P, R, S, †	41
β -Ga ₂ O ₃ or β -Ga ₂ O ₃ :MyOx	Ribbon	10 μ m wide	R	50
β -Ga ₂ O ₃ or β -Ga ₂ O ₃ :MyOx	Plate	8 mm	D, S	39
<i>Ga Oxides on Liquid Metal</i>	Sphere	1-2 nm	S, †	30
<i>Ga Oxides on Liquid Metal</i>	Sphere	30-50 nm	E, S, T, †	31
<i>Ga Oxides on Liquid Metal</i>	Sphere	1-5 μ m	E, M, S, †, ‡	29
<i>GaOOH</i>	Spindles	1-2 μ m	D, F, U	71
<i>GaOOH</i>	Rice/Orzo	250x450 nm	D, F, N, †	58
<i>GaOOH</i>	Rice/Orzo	1-2 μ m	D, F, U,	72
<i>GaOOH</i>	Rod	500-1000 nm	D, E, F, N, S, T, †, ‡, †	73
<i>GaOOH</i>	Rod	100-200 nm	D, F, P, S, U, †, ‡, †	60
<i>GaOOH</i>	Wire/needle	3-1.5 μ m x 300-500 nm	D, U, †	61
<i>GaZnON</i>	Porous Surface	50-100 nm diameter	D, P, T, U, †	65
<i>GaON</i>	Spheroid	50-80 nm crystallite	D, †	9
<i>Gd-Al-Ga₂O₃</i>	Rough Sphere	10-2 nm	D, F, S, U, †	57
<i>Nd:Gd-Ga₂O₃</i>	Sphere/dendrite	30 nm	D, F, S	67

A-Absorption/Emission B-Brunauer-Emmett-Teller D-X-ray Diffraction E-Energy Dispersive X-ray
 F-Fourier Transform Infrared Spectroscopy I – Inductively Coupled Plasma Mass Spectroscopy
 L-Dynamic light scattering M- Atomic Force Microscopy N-Nuclear Magnetic Resonance P-Photoluminescence
 R-Raman S-Scanning Electron Microscopy T-Transmission Electron Microscopy U-Ultraviolet Visible
 spectroscopy †-X-ray Photoelectron Spectroscopy ‡-Selected Area Electron Diffraction † - Differential
 Scanning Calorimetry-Thermal Gravimetric Analysis

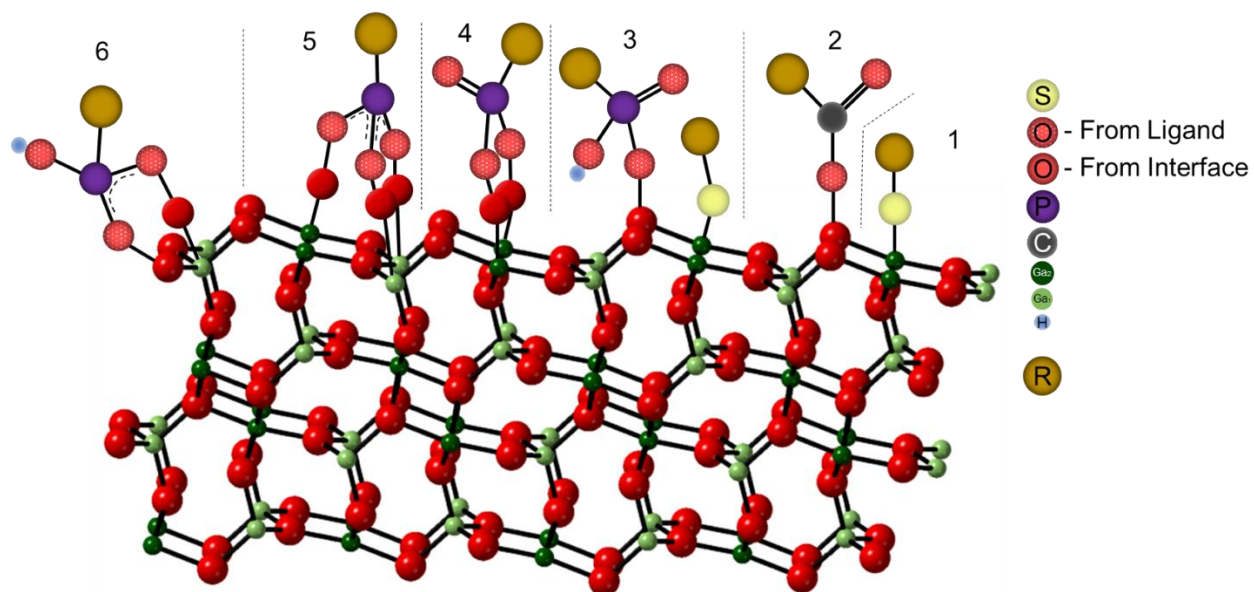


Figure 1.1 Possible binding modes of thiol (1), carboxylic acid (2) and phosphonic acid adsorbates (3 – monodentate; 4, 6 – bidentate; 5- tridentate) to surfaces terminated on Ga containing oxides.

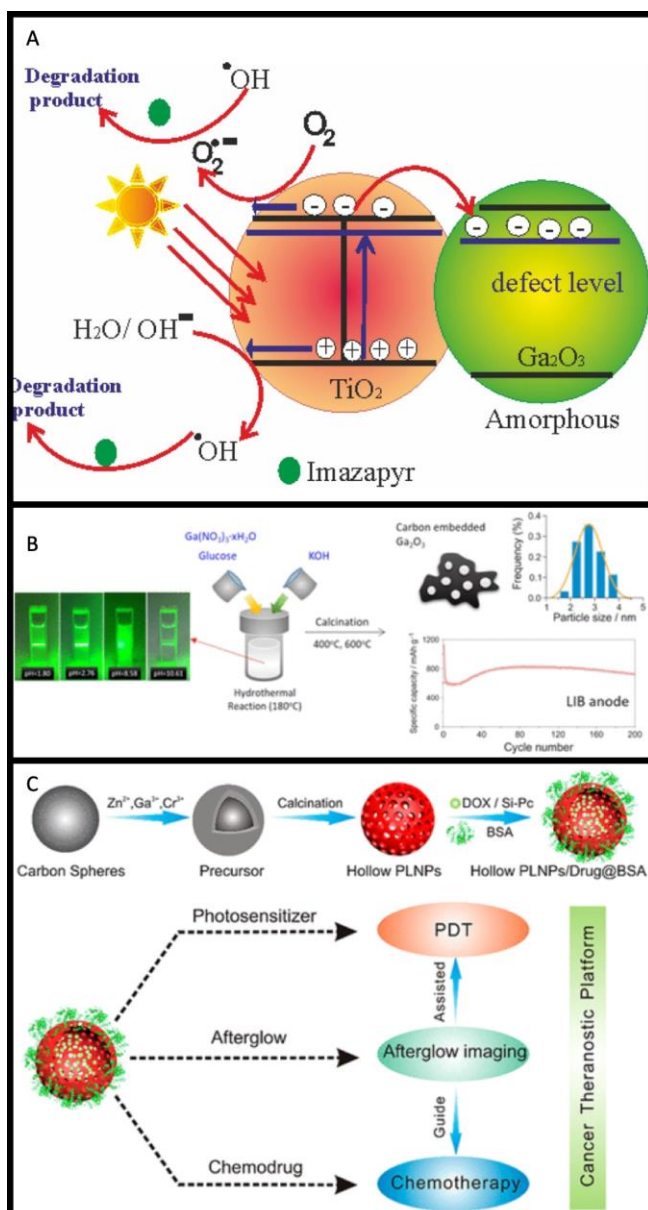


Figure 1.2 Recent applied studies with Ga containing oxides: A) Mesoporous $\text{Ga}_2\text{O}_3\text{-TiO}_2$ nanocomposite for efficient photodecomposition of herbicide imazapyr (copyright 2018 Elsevier); B) Fabrication and testing of Ga_2O_3 anode for lithium-ion batteries (copyright 2018 American Chemical Society); C) Persistent luminous nanoparticles (PLNPs) containing Ga oxides that can be used in cancer theranostic applications after chemical functionalization (copyright 2018 American Chemical Society).

CHAPTER 2

Ga-Ions Enhanced and Particle Shape Dependent Generation of Reactive Oxygen Species in X-ray Irradiated Composites

2.1 Introduction

The imbalance of reactive oxygen species (ROS) in living systems has been connected to potentially detrimental oxidation of biomolecules that can lead to accelerated cell death.⁷⁴ However, if properly managed the generation of ROS can be incorporated into environmental remediation or therapeutic strategies. Thus, materials and conditions that govern the production of ROS are of interest to a number of research communities addressing biomedical or sustainability challenges. Published work with different nanostructured materials has established that many of their specific characteristics can be linked to variable production of ROS.⁷⁵ Size and composition of these types of materials have been initially explored. Size of the nanostructures can lead to variable cell uptake and in turn to different production of ROS.⁷⁶ Shape has also emerged as an additional parameter to consider in explaining variations in ROS levels.^{77,78} For instance, in the case of gold, hexagonal particles produce more ROS compared to spherical and triangular ones during *in vitro* experiments with epithelial cells, but dose, mass and volume also greatly impacted particle cell internalization.⁷⁹ *In vitro* work with carbon materials demonstrated lower ROS levels when spherical shapes were utilized and directly compared to elongated shapes.⁸⁰ In contrast, nanoceria (CeO₂) evaluated in the presence of macrophages produced no ROS regardless of the shape of the material used.⁸¹ However, other oxide materials such as iron oxide do produce variable ROS levels when rod shaped vs sphere shaped ones are placed in the presence of macrophages.⁸² Rod vs spherical nano-sized ZnO have also been studied in cancer cell lines and have generated

variable ROS species.⁸³ The results have been rationalized based on the different stability and release of metal ions from each shape.

The production of ROS can be enhanced not only by the presence of specific materials but also by simultaneous exposure to certain environmental conditions such as radiation. In such situations the maximum effect can be achieved through the use of a scintillator material. A scintillator is any material that can glow when it is exposed to high-energy particles or photons.⁸⁴ X-rays are used to stimulate a scintillator to emit light. The scintillator material is sometimes described as an X-ray transducer that facilitates the generation of $^1\text{O}_2$ through an energy transfer process. A number of medical imaging techniques rely on scintillators and advancements in recent years have been largely due to materials discovery as well as instrumentation improvements.⁸⁵ From a materials prospective the utility of scintillators is based on the fact that they enable the conversion of X-rays to UV/visible photons within 1 ps. The structure, size and composition of scintillators can enhance the desired strong luminescence emission.⁸⁶ Radiation sensitization or radiosensitization refers to a collection of strategies to enhance the effect of radiation exposure.⁸⁷ With respect to biomaterials design that entails the generation of more secondary electrons and increased production of ROS that lead to improved radiation efficacy.⁸⁸ Quantification of the production of ROS after X-ray exposure is one way to benchmark radiosensitization.⁸⁹ Many material systems have been studied to assess their ability to act as radiosensitizers. Promising results with a number of high Z-materials have been published and their references are too numerous to list. However, studies traditionally do not compare architectural configurations with different sizes, shapes and compositions. Designing a biomaterials system that enables such comparisons will facilitate the identification of the most suitable candidates for enhanced radiosensitization that can be further tested in clinically relevant models.

In this paper we examine the role of shape in composites with gallium oxyhydroxide (GaOOH) particles and Matrigel™. The current work builds on prior promising results that demonstrated that the presence of a scintillator material inside a scaffold triggered different cellular response when radiation was used.^{90,91} These studies performed by Berg et al. have demonstrated the behavior of GaOOH nanoparticles in cell free environments of both water and cell growth media. We now study the effect of GaOOH particle anisotropy in a composite. The particles are embedded into the gel in order to understand only the materials effect on the generation of ROS rather than cell penetrating variations, Figure 2.1. Gallium containing nanostructures were chosen for their favorable scintillating properties, documented therapeutic potential of Ga⁹² and recent renewed interest to improve cellular uptake and anticancer activity of Ga– coordinating complexes.⁹³ The inspiration for the design of this current study is based on key prior observations.^{90,91} We observed that in Ga containing composites the ROS production is chemical stemming from the presence of the GaOOH. Therefore, we wanted to test if different shapes of particles with variable stability will produce different ROS amounts. In addition, the design depicted in Figure 2.1 is intended to test if the presence of the any amount of GaOOH can enhance the production of ROS species after variable radiation conditions. We note that in prior work we have also assessed the Ga toxicity using an extremely water-soluble salt: Ga(NO₃)₃.⁹¹ Previously, we recorded no concentration dependence on toxicity. In this work we test the effects of the collective behavior hypothesized to contribute to the production of more ROS and result in an enhanced radiosensitization. The GaOOH particles are characterized by scanning electron microscopy (SEM) and X-ray diffraction (XRD). We evaluate the stability of GaOOH in solution by recording the amount of metal leached using inductively coupled plasma mass spectrometry (ICP-MS). The amount of ROS in each construct under variable radiation conditions is quantified

in the presence and absence of cells seeded on top of the composites. The viability of cells is also recorded under different *in vitro* conditions. The collective materials characterization and the results from the bioassays are used to explain the role of anisotropy on the radiosensitization of nanostructures containing Ga.

2.2 Results and Discussion

We focus on understanding how to enhance the radiosensitization effect during the fabrication of the composite rather than exploring ideas to increase the effect via better uptake of particles into cells. We prepared three composites with different arrangements, shown in Figure 2.1, in order to test the following hypotheses: 1) Composition and amount of Z-material in the composite determines the magnitude of the radiosensitization; 2) Anisotropy of the nanostructured material in the composite has an effect on the generation of ROS; 3) Material composition and anisotropy can be used to generate additive or cooperative effects. We synthesized two different shapes of GaOOH and also used commercially available gallium salt, $\text{Ga}(\text{NO}_3)_3$ that is highly soluble in water. We chose these Ga-containing materials because even small quantities of Ga can have noticeable impact. It is known that gallium ions can bind to transferrin receptors and be taken specifically and non-specifically into cells.⁹² This can result in severe disturbance of iron homeostasis and have adverse effects.⁹⁴ The amount and shape of the Ga-based material are controlled during the composite manufacturing. The composite fabrication requires no specialized equipment and only easy processing that relies on different Ga mass quantities to vary the properties of the composite. PC12 cells were used to study the production of ROS before and after radiation. During all testing, the cells were seeded on top of the GaOOH/ Matrigel™ composites to avoid endocytosis of GaOOH nanostructured material. No visible particles were identified on the top of the interface. In the experimental set-up we also performed experiments in the absence

of cells. This set-up permitted us to understand the ROS changes induced by the Ga-based materials in the composite after radiation rather than changes as a result of transformations due to dynamic biological processes driven by the cells.

A number of research groups have published reports on how to synthesize GaOOH via solvothermal procedures.⁹⁵⁻⁹⁷ We choose to utilize a microwave synthesis method because: the synthesis can be finished in less than an hour; the starting material, GaNO₃, is commercially available and affordable for a large-scale synthesis; the size and shape of the nanostructured product can be varied by tuning the reaction conditions; and the resulting particles do not require any stabilizing ligands. In a typical synthesis run we dissolved GaNO₃ in water to create a 0.1 M solution. We increased the pH to 8 by slowly adding NaOH. That solution is then loaded into a glass vessel and placed into a microwave synthesis system and heated to 120 °C for 20 min. The product that forms is fluffy and white in color. This product is washed with water and vacuum dried with no heat. During the entire procedure no organic ligands are used to control the size and shape of the particles. One can change the shape by simply omitting the use of heat to allow the formation of GaOOH. The quality of the particles was assessed with a number of characterization techniques. Thorough examination of particle shape and morphology was performed with SEM analysis and representative images are shown in Figure 2.2. The SEM characterization was performed in order to assess size and shape, and not to assess aggregation behavior. We termed one shape of particles as orzo due to its specific elongated geometry with the appearance of stacked (lenticular) plates that comprise the overall ovoid shape. The other shape is referred to as anisotropic and was observed to be granular with random nanoscale features on each side of its blocky, sub-angular structure. XRD was used to track the transformation of GaNO₃ (an amorphous material) to crystalline GaOOH by looking at the shape (broad for amorphous) and sharp (for

crystalline) of the peaks in the spectrum, Figure 2.3. Use of the Scherrer's equation provides a way to compare the two types of particles synthesized. Since peak width is inversely proportional to crystalline size we analyzed data collected for both shapes and the peak at the (110) direction. Calculations done using the Scherrer's equation and the peak at the (110) direction showed that the crystalline grains for the orzo shape are ~49 nm and for the anisotropic one to be ~53 nm. In addition, we confirmed that the diffraction patterns on Figure 2.2 can be assigned to the orthorhombic GaOOH structure and are in agreement with literature reports.²⁷

Nanostructured-Matrigel™ composites for all testing of the stated hypothesis were prepared by mixing either the GaOOH particles or the Ga(NO₃)₃ salt with Matrigel™ and cell medium. All of the compositions were placed in standard 96 well plates. The compositions contained the following concentrations of Ga-based material: 0.02 mg/μL, 0.04 mg/μL and 0.08 mg/μL (See supporting information for plate design for each bio-assay). Each plate was irradiated using a 6 MV photon beam from a clinical linear accelerator (Novalis TX; Varian Medical Systems, Palo Alto, CA, USA). Prior to the irradiation experiments the plate was surrounded by at least 1 cm of solid, homogeneous, tissue-equivalent bolus material (density of 1.03 g/c). The set-up is essential in order to achieve buildup of lateral electronic equilibrium. Prior to every experiment each plate as placed at least 2 cm from the edge of the radiation field to minimize penumbra effects. In addition, we covered the cell culture dishes with 8.9 cm solid water phantom material which was necessary to guarantee the maximal field flatness. The output rate was set to 200 MU min⁻¹ (SAD = 100 cm, d = 10 cm, A = 15 x 15 cm²). The samples inside the cell culture dishes received total doses of 2, 4, or 10 Gy in a single fraction.

We chose to utilize the PC12 cell line due to the ease of handling and the abundance of studies published in the literature utilizing the same *in vitro* protocols.⁹⁸ The procedure for the

growth of PC12 cells utilized Dulbecco's Modified Eagle Medium (DMEM) high glucose formulation, with 12.5% horse serum, 2.5% fetal bovine serum, and 1% penicillin-streptomycin. The conditions for the incubation were 37°C and 5% CO₂ in a humidified incubator and were maintained throughout all experiments. The parameters for each trial were 7.5 x 10⁴ cell/mL density and 0.5 mL per 100 mm plate. We allowed the PC12 cells to adhere for 18 hours prior to beginning each trial. Control experiments were performed on gels with no Ga material. We assessed cell survival (Alamar Blue assay) and ROS generation (DCFH-DA assay). Figures 6 and 4 summarize the results from the cell assays. Due to the number of parameters and comparisons, all statistical analysis is reported in the supporting information. Here we present a summary of the statistically significant interactions that were observed, along with key conclusions we made based on the recorded results and subsequent statistical assessment.

In experiments performed on Matrigel™ with no Ga-containing materials we observed a small decrease in cell viability with time when the PC12 cells were not exposed to any radiation treatments. Some cell death is expected as the amount of cells grows with the duration of the experiments progresses as seen in Figure 2.4. When these samples were exposed to radiation, increasing radiation exposure resulted in no significant changes in cell survival as the days of the experiments progressed, Figure 2.4. We observed very different results in viability when the 3 types of Ga-containing materials were added to the composite, Figure 2.5. The Ga-salt yielded statistically significant decrease in viability as both the concentration and the radiation dose increased. In the case of the orzo particles the viability of PC12 cells changed only at higher concentrations, and the amount of radiation did not influence the cell survival significantly. In contrast, the anisotropic particles contributed to a decrease in cell viability based on increasing concentration and a smaller decrease based on higher doses of radiation treatment. Literature

reports have established that the levels of tolerance for Ga ions in different living systems are yet to be established but evidence points to the conclusion that the lethal toxicity of Ga³⁺ is significantly lower than other metal ions.⁹⁹ Our viability results support this conclusion since we observed significant changes only at increased concentrations. The radiation exposure decreased the viability of the PC12 when a significant amount of Ga was present in the system supporting the notion that this metal can have a radiosensitizing effect.

We quantified the amount of ROS under different radiation conditions in the presence and absence of cells, Figure 2.6. The presence of ROS causes breaks in the DNA structure and leads to cell apoptosis and is used as a measure of radiosensitization. The fluorescence at different time points (days) was recorded. The DCFH-DA was dissolved in DMEM at a concentration of 60 μ M. For each measurement, the cell media was aspirated off and 1 mL of the DCFH-DA solution was added. An incubation time of 30 minutes was used prior to the fluorescence measurements with a Tecan GENios microplate reader. The excitation filter and emission filters were at 485 nm and 535 nm, respectively. The use of DCFH-DA in cell free experiments has been the subject of other published work that showed that with proper control experiments one can utilize the results obtained by this assay to understand factors that influence the generation of ROS in solution.^{100,101} We first consider the data obtained in the absence of cells, 1st row of plots on Figure 2.6. In the case of the gallium salt, we recorded an increase in ROS production with an increase in concentration and eventually saw a saturation effect at the highest concentration. When the samples containing the gallium salt were exposed to radiation at different doses we only observed an initial significant change in ROS production, and no change was observed as the days of the experiment progressed. In the case of the orzo particles we observed a decrease in ROS production with higher concentrations and higher doses in radiation. However, with the anisotropic particles

higher concentrations and higher doses in radiation yielded more production of ROS. Overall, the results we recorded in the absence of cells support the notion that the orzo particles are more stable in solution and release less gallium ions that can cause the production of ROS. The data recorded with the anisotropic shape gave trends similar to the ones collected with the water-soluble $\text{Ga}(\text{NO}_3)_3$ supporting a conclusion that this shape of GaOOH is highly unstable in aqueous solutions which can induce ROS production.

The ROS assay was performed in the same manner after cells were seeded on the same composites and exposed to the same radiation conditions, second row of plots on Figure 2.6. We observed the same overall comparative trends in ROS production as we did when there were no cells present, though the amount of ROS measured was different compared to the data when no cells were present. The results from both bioassays suggest that the availability of Ga ions in solution is the main reason for the observed changes after radiation exposure with respect to cell viability as well as ROS production. We tested the stability of the two types of GaOOH by incubating them in cell media, filtering the particles out and measuring the amount of Ga leached by ICP-MS. All the data along with standard deviations is plotted and presented in the supporting information. Table 2.1 shows a comparison between the two trends of behavior we recorded. We observed that the anisotropic particles continued to release Ga in solution as the days of the experiment progressed. In contrast, the amount of Ga released from the orzo particles drastically decreases as the material was incubated in solution for 3 days. The data in Table 2.1 supports the notion that placement of the orzo particles in solution for longer periods of time leads to passivation of their surface. Taken in sum the data collected by ICP-MS supports the conclusions from the ROS and viability assays and confirm that two types of particles have different stability in solution. Thus, the overall trends in ROS production based on concentration and radiation conditions were

governed by particle stability. Leached amount of Ga coupled with radiation dose can be used to generate different amounts of ROS during *in vitro* experiments.

Table 2.1 Summary of differences in the amount of Ga leached compared to the initial value on day 0 immediately after placing the particles in solution.

<i>GaOOH</i> type	Day 1	Day 3
<i>Orzo</i>	- 24 ± 0.5 %	- 52 ± 2.2 %
<i>Anisotropic</i>	+149 ± 26.2 %	+454 ± 14.8 %

2.3 Conclusions

In summary, we demonstrate that the presence of Ga ions in composites can have a radiosensitizing effect during *in vitro* experiments with PC12 cells. We confirmed our hypothesis that the amount of the available Ga³⁺ determines the magnitude of the radiosensitization. With respect to shape of the GaOOH particles, one observes changes in the generation of ROS which are related to the stability of the specific shape in aqueous solutions. Further, our results support the notion that concentration and shape of Ga containing materials can be combined to generate an additive effect by increasing the amount of available free metal ions in solution. The metal ions contribute to the greatest generation of ROS after exposure to ionizing radiation. The studies with GaOOH containing composites enable one to explore the role of key parameters that lead to an increased efficiency of radiation treatments. The reported results are currently being considered in our laboratories for further translational biomaterials approaches.

2.4 Experimental Section

Materials: The gallium nitrate hydrate (289892) was obtained from Sigma Aldrich. Phenol red free Matrigel (354262) and sodium hydroxide (UN1823) were obtained from Fisher Scientific. The Alamar Blue assay (DAL 1025) was supplied by ThermoFisher Scientific. The ROS assay uses 2',7'-Dichlorofluorescein diacetate (DCFH-DA) and was utilized as received from Sigma-Aldrich.

Ga particle fabrication: The orzo GaOOH nanoparticles were synthesized via a microwave reaction based on an experimental procedure reported by Pearce et al.²² The anisotropic GaOOH nanoparticles were synthesized by precipitating GaOOH from solution with no additional microwave or thermal treatment.

Composite preparation: The Matrigel™ composite was prepared by following the thin gel protocol provided by Corning and diluting to a protein concentration of 3 mg/ml. The gallium bearing material was mixed with Matrigel™ just after pipetting into cell culture plates to ensure homogeneity before gelation.

SEM characterization: All samples were evaluated using the FEI Verios 460L in AIF. The Everhart-Thornley detector was used in backscatter mode with an accelerating voltage of 2kV and a sample current of 13pA.

XRD characterization: XRD analysis was performed with a Rigaku SmartLab X-ray diffractometer. Powder diffraction was done with a CuK_α X-ray source at 40kV and 40mA with Bragg-Brentano optical set up.

Cell Culture and Bio Assays: Culturing of PC12 cells was done using a sterile technique and a protocol described in prior work.¹⁰² Cells were kept in an incubator at 37 °C and the cell

media was replenished every 48 hrs. The bio assays were carried out using the manufacturer's protocol and details for each one have been reported elsewhere.¹⁰³

ICP-MS: The samples incubated in the two shapes of GaOOH was filtered and analyzed for gallium amount with a Perkin Elmer Sciex Elan DRCII ICP-MS. Prior to any data collection a calibration was done with gallium 69. The solutions were also diluted before the analysis and the dilutions are factored in the final values of the leached Ga.

Radiation Exposure Experiments: All plates were irradiated with 6 MV photon beam from a clinical linear accelerator (Novalis TX; Varian Medical Systems, Palo Alto, CA, USA). Experimental details have been detailed in Berg et al.¹⁰⁴

Statistical analysis: All statistical analyses were conducted using OriginPro 2016 (b9.3.1.273). One-way and two-way ANOVAs were used to find differences between the experimental conditions with a significance level of 0.05.

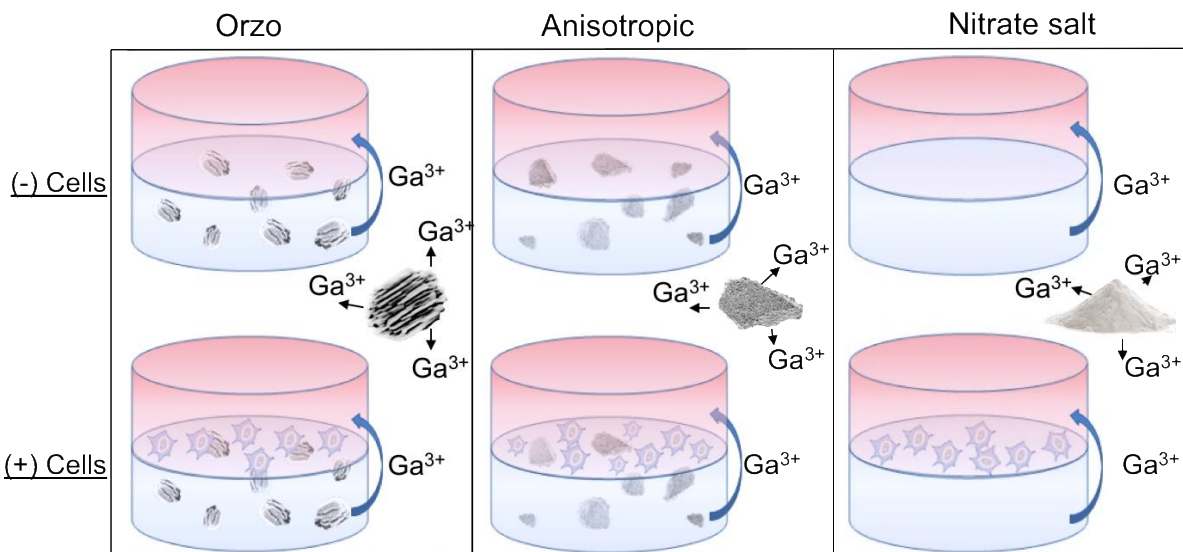


Figure 2.1 Representation of the approach used to test the role of shape of GaOOH particles on PC12 cell viability and ROS production.

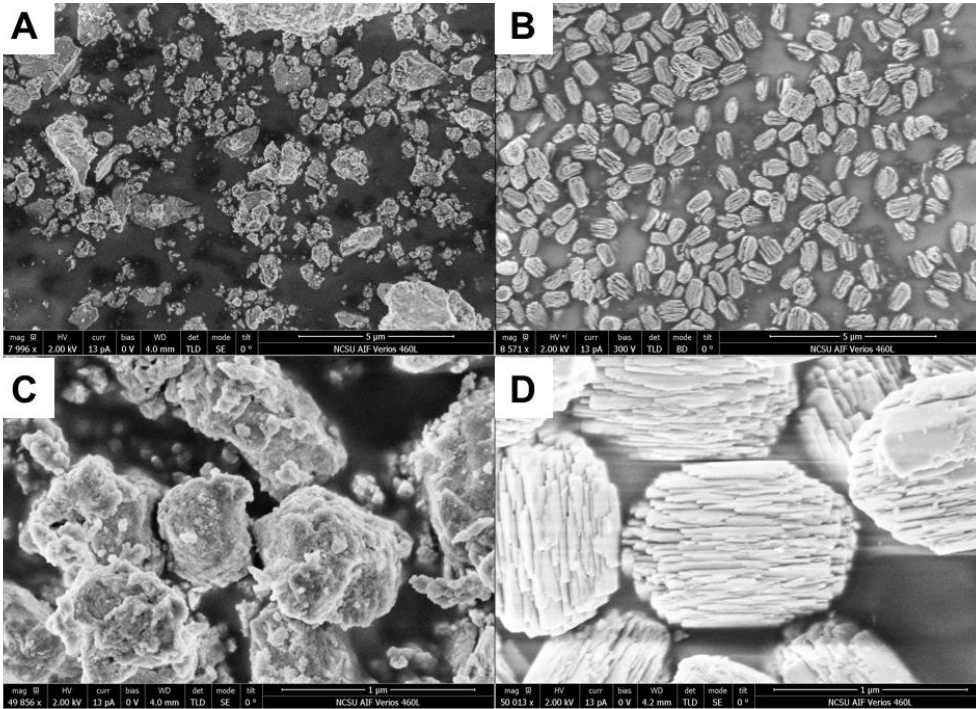


Figure 2.2 Representative SEM images of the different shapes of GaOOH used in the study: A) anisotropic and B) orzo. Parts C) and D) show zoomed in structures for the anisotropic and orzo shapes, respectively.

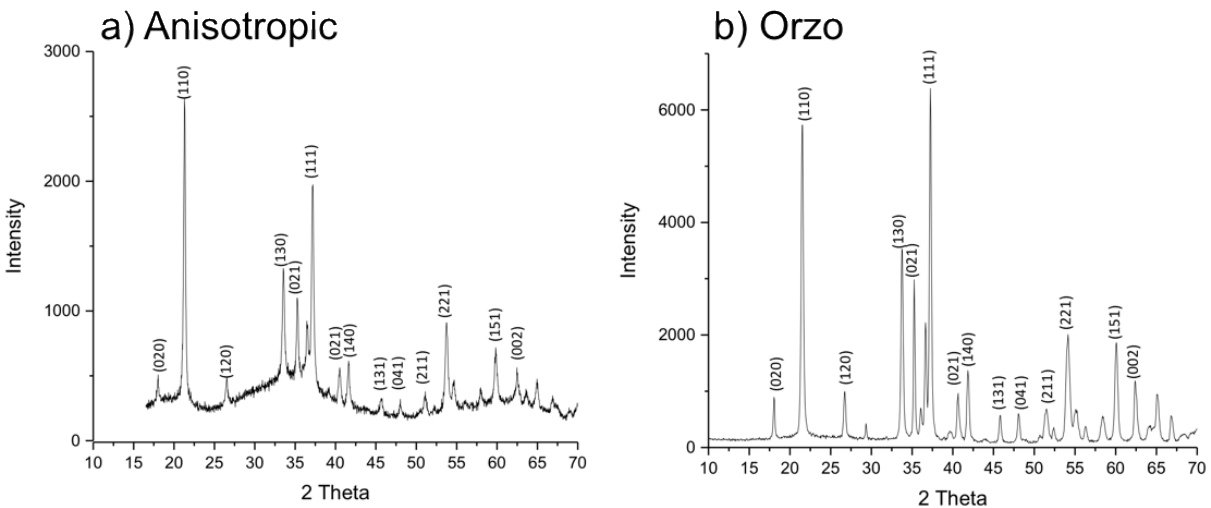


Figure 2.3 XRD characterization of the different Ga containing materials used in the study: a) anisotropic GaOOH particles and b) orzo GaOOH particles.

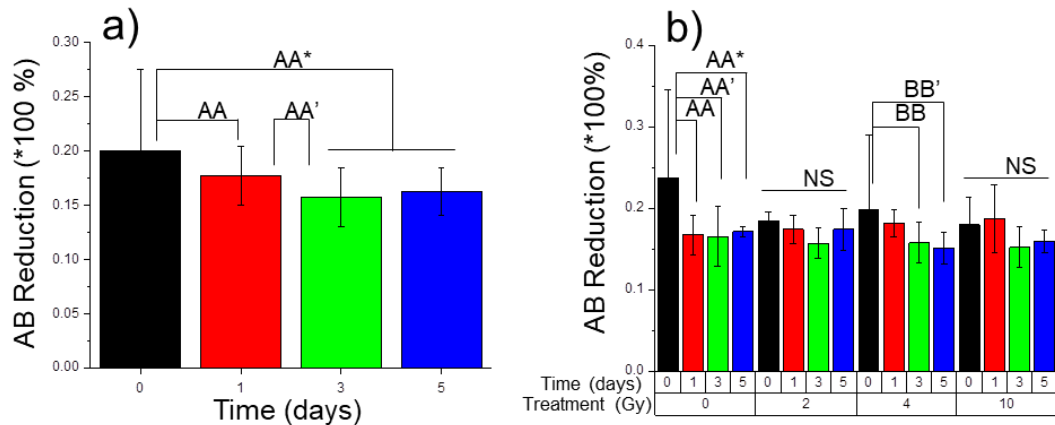


Figure 2.4 Cell viability assay results in the absence of GaOOH material: a) AB assay conducted in the presence of no material, just Matrigel; b) AB assay conducted in the presence of no material and after the indicated radiation treatment.

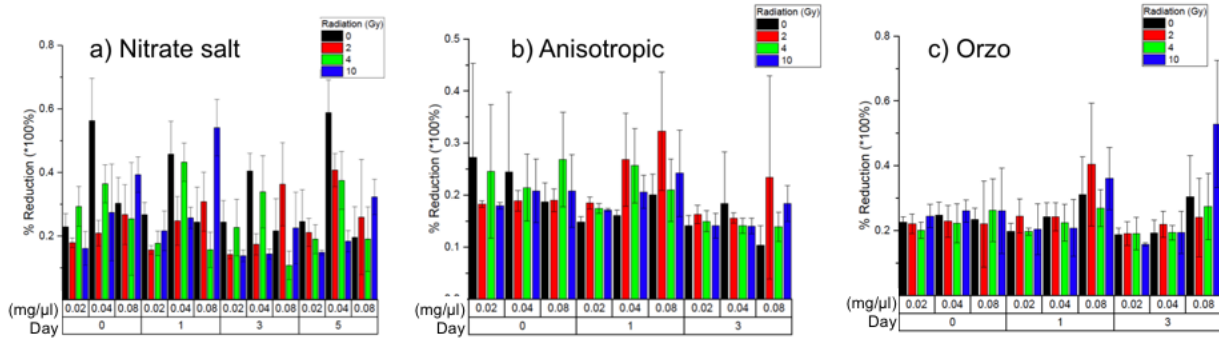


Figure 2.5 Summary of the cell viability assays performed with Alamar Blue after the indicated times in days, exposure to different amount of radiation and in the presence of the specified concentrations of a) nitrate salt; b) anisotropic GaOOH; and c) orzo GaOOH.

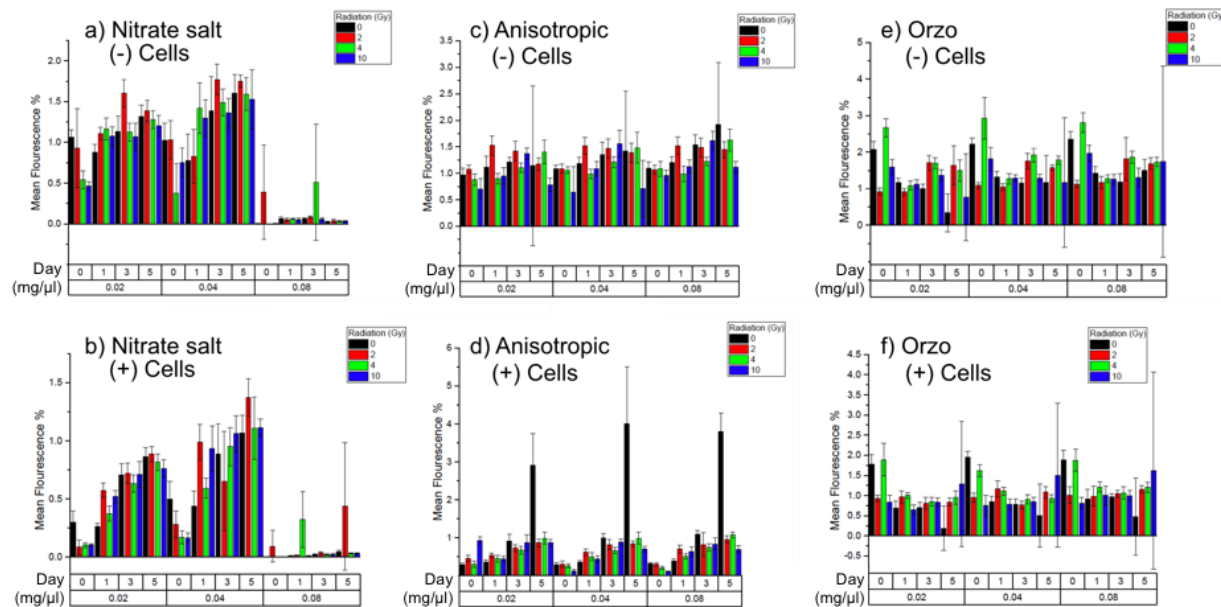


Figure 2.6 Summary of the ROS assays performed with DCFH-DA after the indicated times in days, exposure to different amount of radiation and in the presence of the specified concentrations of a) nitrate salt; b) nitrate salt and PC12 cells seeded on top of the Ga containing composite; c) anisotropic GaOOH; d) anisotropic GaOOH and PC12 cells seeded on top of the Ga containing composite; e) orzo GaOOH; f) orzo GaOOH and PC12 cells seeded on top of the Ga containing composite.

CHAPTER 3

Nanostructured GaOOH modified with reactive yellow, red and blue water-soluble dyes

3.1 Introduction

Water soluble reactive dyes are used to modify nanostructured GaOOH. The resulting particles showed excellent stability in water solutions. The materials were characterized by Scanning electron microscopy (SEM) and X-ray Photoelectron Spectroscopy (XPS) to assess changes due to the dye functionalization. SEM revealed changes in size after dye modification. XPS confirmed the presence of the dyes on the nanostructured materials and assessed changes in functional groups due to use of different type of modification and concentrations of dyes. The reported approach to stabilize the nanostructured GaOOH provides a simple and environmentally friendly route to tune the properties of wide band gap semiconductor materials.

Reactive dyes are water-soluble dyes capable of entering into a chemical reaction with the hydroxyl groups of cellulose, to become covalently bonded to the cellulosic fibers. These dyes are mostly used with cotton but they can also be applied for wool and nylon fibers. In general, a reactive dye consists of an electrophilic reactive group that contains a leaving group, a bridged linker, the chromogen, and one or more water solubilizing groups.¹⁰⁵ Taken in sum these attributes render reactive yellow, red and blue dyes ideal for surface functionalization of oxide materials. In particular, nanostructured oxides are increasingly in need of chemical functionalization in order to increase their utility in applications ranging from energy storage devices to biomedical imaging.¹⁰⁶ Surface modifications can have passivating effects on particles' shape, stability and dispersal in solution.¹⁰⁷ In this work we seek to alter gallium oxyhydroxide (GaOOH) nanostructures²² via modification with reactive water-soluble dyes in order to improve their stability in aqueous solutions.

3.2 Synthesis

We have previously reported on the synthesis of GaOOH.¹¹ Prior to the synthesis a solution containing a gallium salt is prepared and heated, NaOH is added until the pH reaches 8 and a white precipitate is formed. Four different reactive dyes were utilized, Figure 3.1: (i) tetrasodium;(3Z)-5-[[4-chloro-6-(3-sulfonatoanilino)-1,3,5-triazin-2-yl]amino]-4-oxo-3-[[4-(2-sulfonatooxyethylsulfonyl)phenyl]hydrazinylidene]naphthalene-2,7-disulfonate (Color Index (C.I.) Reactive Red 198 (RR198), one chlorotriazine and one vinyl sulfone reactive group), (ii) trisodium;7-[[2-(carbamoylamino)-4-[[4-[2-(2-ethenylsulfonylethoxy)ethylamino]-6-fluoro-1,3,5-triazin-2-yl]amino]phenyl]diazanyl]naphthalene-1,3,6-trisulfonate (C.I. Reactive Yellow 174 (RY174), one vinyl sulfone reactive group), (iii) disodium;1-amino-9,10-dioxo-4-[3-(2-sulfonatooxyethylsulfonyl)anilino]anthracene-2-sulfonate (C.I. Reactive Blue 19 (RB19), one vinyl sulfone reactive group), and (iv) 1-amino-4-((3-((4-chloro-6-((3-sulfonatophenyl)amino)-1,3,5-triazin-2-yl)amino)-2,4,6-trimethyl-5-sulfonatophenyl)amino)-9,10-dioxo-9,10-dihydroanthracene-2-sulfonate (C.I. Reactive Blue 49 (RB49), one chlorotriazine reactive group). We carried out the chemical modification via in-situ and ex-situ protocols. The ex-situ treatment begins by synthesizing a large batch of GaOOH particles in clean water with Ga(NO₃)₃ as the precursor for the hydrothermal conversion, followed by drying, and subsequent separate exposure to each dye in solution. A representative image of the particles is shown in Figure 2.3. Three different concentration ranges were tested: μM, nM and pM. In the second approach, the in-situ procedure, the GaOOH particles were synthesized under the same hydrothermal conditions but with dye in solution and were subsequently dried. The high crystallinity of the dye modified GaOOH particles was verified by X-ray diffraction (XRD) and matched prior reports.

3.3 Discussion

The stability of the nanostructured material was tested in water solutions.¹⁰⁸ The particles were dispersed in water and allowed to soak for up to 72 hours. The samples were then centrifuged in Nanosep 300k Omega centrifuge vials to separate the leachate from the GaOOH. The leachate was analyzed by Ultraviolet-visible spectroscopy (UV-VIS) and the resultant spectra were compared to the spectra of dye solutions of known concentration. We observed no detectable amounts of dye leaving any of the samples we synthesized. In addition, we also soaked and sonicated the samples for 2 hours to further test the leaching of dyes. Despite the sonication, we again observed no leaching of dyes. The result supports the notion that the dye modified nanostructured GaOOH particles are remarkably stable in aqueous solutions, an important property for a number of applications.¹⁰⁹

We carried out a detailed characterization to rationalize the stability of the functionalized GaOOH particles. The morphology and the size of the material were examined by a Tescan MAIA3 field-emission scanning electron microscopy (SEM) and the composition was analyzed by AXIS Supra X-ray Photoelectron Spectroscopy (XPS). Survey XPS spectra and high-resolution C 1s, O 1s, Ga 3d, N 1s and S 2p core level spectra were measured using monochromatized Al K α radiation (1486.6 eV, probe area is $0.7 \times 0.3 \text{ mm}^2$, energy resolution is 0.45 eV). Charge compensation was used during XPS spectra acquisition. The chemical composition of the film surface was determined from the corresponding photoelectron peak areas after standard Shirley inelastic background subtraction and by using the relative sensitivity factor method. The high-energy resolution core level peaks were fitted by using Gaussian functions. All spectra were calibrated to the C 1s peak position at 284.8 eV.

The samples were prepared by adhering small amounts of powder to double sided conductive carbon tape on a microscope slide. Table 3.1 summarizes the SEM analysis and one can conclude that the use of water-soluble dyes for modification of GaOOH has a measurable effect on particle morphology and size. A 3-way ANOVA analysis was performed on the particle length, width, and length to width (L/W) ratio data collected via SEM measurements. There was significant difference ($p < 0.05$) between the materials prepared by ex-situ and in-situ methods. Furthermore, the clean GaOOH samples resulted in the longest and widest particles (LxW is up to 1311x685 nm) and while the ex-situ treatment presented the smallest particles (down to 330x160 nm).

In the case of RR198 in-situ treatment, there was a statistically significant difference between the μM and nM (also between the μM and pM) concentrations with the particle decreasing in size as concentration decreased. RR198 ex-situ treatment led to a similar trend with a significant difference between μM and nM concentrations; with particle size decreasing as concentration decreased. The RB19 in-situ treated samples showed no statistically significant difference between concentrations. However, when the p-value was changed a difference between samples treated with both the μM and nM as well as the pM was observed. In contrast, for the ex-situ case, there is no statistically significant difference between particle sizes as dye concentration changed. The RB49 in-situ treated sample presented no statistically significant difference in particle length and width as dye concentration changed. For the same dye the ex-situ sample showed a statistically significant difference between μM and both nM and pM concentrations with an increase in particle length and width as dye concentration decreased. Furthermore, there was no significant difference between the ex-situ and in-situ treatments for the dye RB49. For the RY174 in-situ treatment, the particles showed a significant difference between μM and pM concentrations with particle size

decreasing as dye concentration decreased. The ex-situ treated samples resulted in no significant difference in particle size with respect to changing of dye concentration. Similarly, there was no significant difference between ex-situ and in-situ treatments for the dye RY174.

Changes in the surface chemistry of the nanostructured GaOOH were assessed by XPS. A summary of the elemental compositional changes is shown in Figure 3.3. Upon dye functionalization we observed the presence of sulfur as compared to clean particles and changes in the relative amounts of the other elements present. We deconvoluted the C 1s and O 1s high resolution data due to the abundance of O and C in the dye molecular structures and for the purpose of assessing changes among the different types of samples we prepared. Comparative summaries can be seen in Table 3.2 and Table 3.3. A Monte Carlo area quantification error analysis was done on the deconvoluted C 1s spectra. The mean peak area and standard error were used to examine statistically significant differences in bond percentage with respect to changes in dye concentration and treatment method. Three bond types were analyzed: C-C (binding energy of 285.0 eV), C-O (286.5 eV), and C=O (288.0 eV).¹¹⁰

In the case of RR198 ex-situ and in-situ treatments, there was a statistically significant difference in C-C bond relative concentration (%) between the nM and pM concentrations and the C-C bond concentration of clean particles. The only other significant difference was observed between the in-situ treated samples with μ M and nM concentrations with C-C% decreasing as dye concentration decreased. The RB19 ex-situ treated sample showed a significant difference when treated with the μ M and nM concentrations with C-C% increasing as dye concentration decreased. There was significant difference between in-situ and ex-situ treatments at the μ M and pM concentrations with the ex-situ sample having a lower C-C% bond concentration. There seems to be no statistically significant difference in C-C% as dye concentration changes in either treatment

for RB49 at the μM concentration. However, there was a significant difference between ex-situ and in-situ treatments at the nM and pM concentrations. The RY174 ex-situ treated sample showed a significant difference when treated with μM and pM concentrations with C-C% decreasing as dye concentration decreased.

The only group to have any statistically significant differences between C=O% bond concentration was on RB49. The ex-situ treatment showed a difference between both the μM and pM and nM concentration with a spike in C=O% at the nM concentration. The only significant difference in C-O% that RR198 showed was between the in-situ treatments with μM and pM concentrations with C-O% increasing as dye concentration decreased. The RB19 in-situ treated samples all showed significant difference in C-O% bond concentration as compared to the clean GaOOH particles with the dye modified particles having a lower C-O%. The ex-situ treatment with μM and nM concentrations also showed a significant difference in C-O% when compared to the clean sample. The RB49 in-situ treated sample showed a significant difference between all concentrations with a sharp dip in C-O% when using nM concentration and an increase in C-O% when using μM to pM concentration. The ex-situ treated sample showed a significant difference between all concentrations with a dip in C-O% when using nM concentration and a decrease in C-O% when using the μM to pM concentration. There was no statistical significance in any of the RY174 samples.

The same type of Monte Carlo area quantification error analysis was also done on the deconvoluted O 1s spectra. Three bonds were examined, namely O-C, O-Ga, and O=C.¹¹¹ There were very few significant interactions for the O-C% peaks. The only significant interaction among the RR198 samples was observed in the spectra of samples RR198 treated in-situ with μM and pM concentrations with the O-C % increasing as dye concentration decreased. RB49 ex-situ showed

significant interactions between $\mu\text{M}/\text{nM}$ and pM concentration with O-C% decreasing as dye concentration decreased. RB19 ex-situ showed a significant difference between μM and nM concentration with a spike in O-C% at the nM concentration that returns to normal at the pM level. RY174 presented no significant differences in O-C%.

RR198 and RB19 were the only two dye treatments that led to a significant difference in O-Ga% bond concentration. RR198 treatment led to a significant difference in O-Ga% bond concentration between the ex-situ and in-situ treated samples. The RR198 treated sample showed significant interactions between all concentrations with a sharp dip in O-Ga% when treated with nM concentration with decreasing O-Ga% as dye concentration decreased. The only significant interaction change was seen in RB19 ex-situ and in-situ treatments with nM concentration with the in-situ sample showing higher O-Ga% bond concentration. The RR198 in-situ treatment led to a significant difference of O=C% bond concentration between samples treated with μM and pM concentrations and with nM concentration, with a spike in O=C% at the nM concentration. There was also a significant difference between in-situ and ex-situ treatments of samples treated with μM and pM concentrations with the in-situ treated samples presenting lower O=C% than ex-situ treated ones.

RB49 dye presented significant interactions for the ex-situ treatment with both μM and pM concentrations and pM concentration with the O=C% increasing at the dye concentration decreased. The RB19 ex-situ treatment led to a significant difference in the bond concentration of samples treated with μM and with both μM and pM concentrations, with O=C% increasing as dye concentration decreased. The in-situ treatment showed a significant difference when using nM and pM concentrations with a dip in O=C% at the nM concentration. The RB19 treatment also led to a significant difference in bond concentration of the samples treated in-situ and ex-situ with nM

concentration with the ex-situ treated samples tending to have a higher O=C% bond concentration. The RY174 treatment led to no significant differences in O=C% bond concentration for any testing conditions.

3.4 Conclusion

In summary, our analysis showed that the GaOOH particle size can be modulated via functionalization with water soluble reactive dye molecules. One can carry out the modification via two very easy methods without the need for high temperatures or specialized equipment. The in-situ and ex-situ route can result in different amounts of chemical species on the surface of the nanostructured GaOOH. Our stability experiments and compositional study by high resolution XPS analysis support the notion that the dye molecules are layered on the particle surface rather than anchored via a specific functional group. Our current efforts did not focus on controlling this layering of dyes on the particles' surface, but this can be the subject of future studies in order to tune additional materials' properties such as transparency.

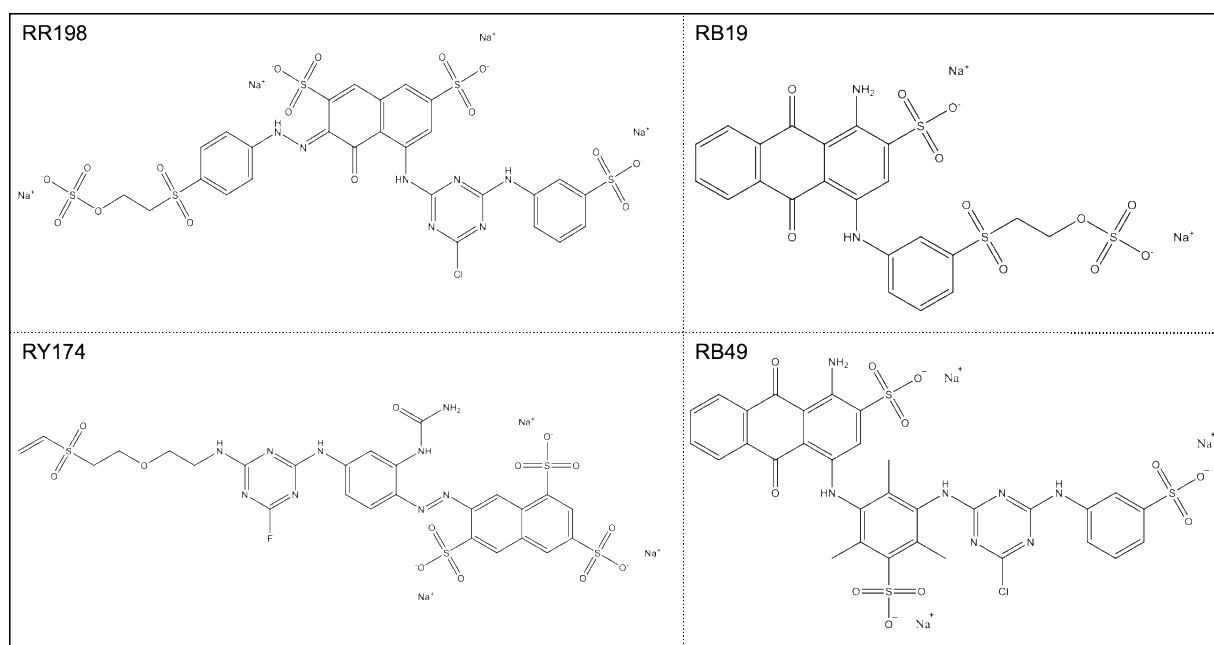


Figure 3.1 Chemical structures of the four different dyes.

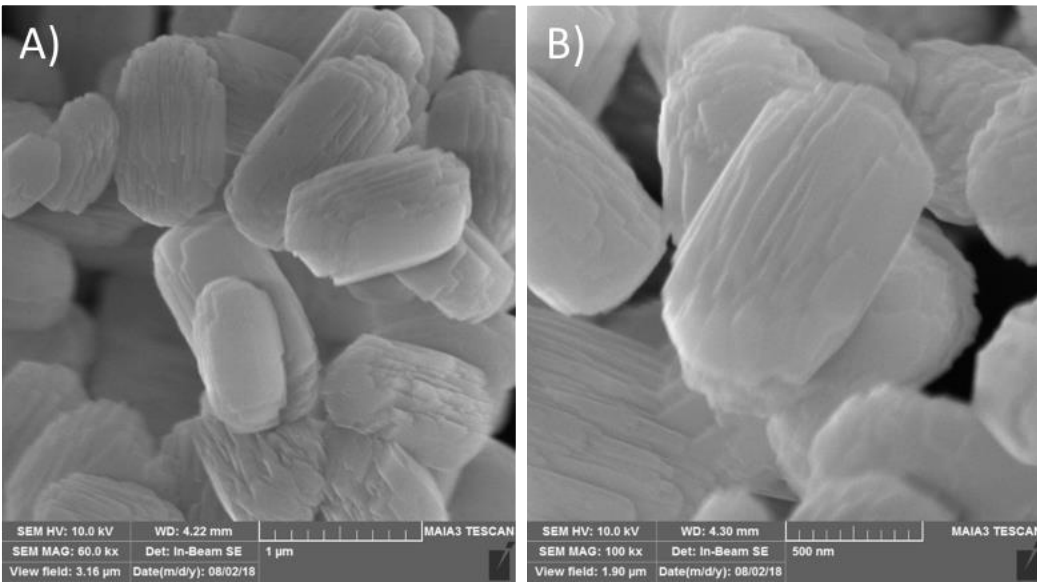


Figure 3.2 GaOOH particles at A) 60kx magnification B) 100kx magnification.

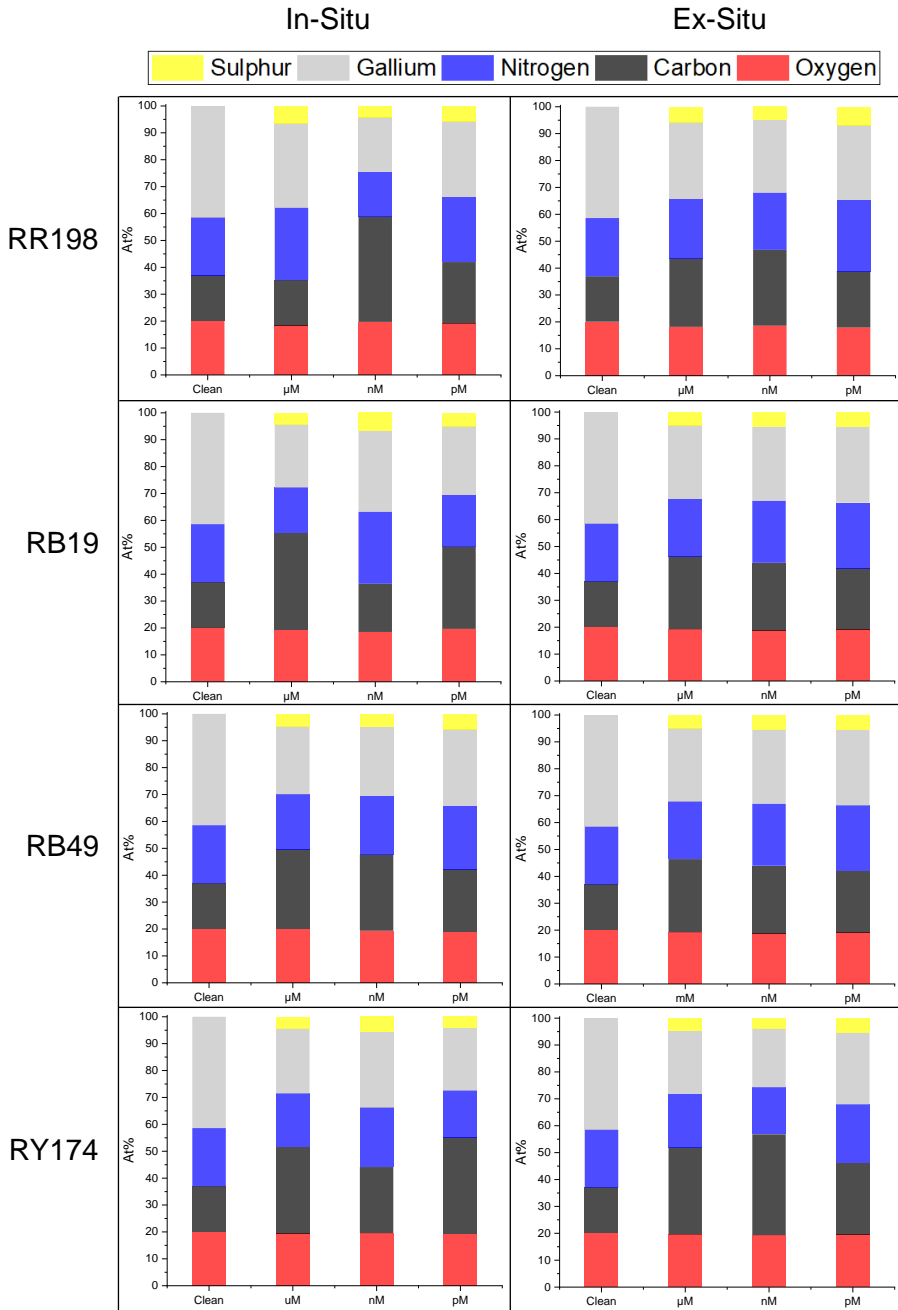


Figure 3.3 Comparison among elemental compositional changes extracted from XPS data.

Table 3.1 Summary of SEM Analysis of the Synthesized Materials

	In-Situ			Ex-Situ		
	L/W	Length±ST DV (nm)	Width±STD V (nm)	L/W	Length±STD V (nm)	Width±STD V (nm)
RR198 μM	2.17±0.29	913±111.7	420±22.8	1.84±0.07	437±4.7	237±12.5
RR198 nM	1.63±0.21	306±27.3	187.6±18.1	1.67±0.15	390±29.4	233±23.5
RR198 pM	1.78±0.075	313±10.2	175.6±4.9	2.08±0.25	430±16.3	207±4.7
RB19 μM	2.23±0.24	860±92.0	385±10.8	1.67±0.13	345±24.8	207±34.0
RB19 nM	2.30±0.077	967±20.6	420±17.9	1.85±0.35	370±29.4	200±16.3
RB19 pM	1.98±0.16	606±33.7	306±30.9	1.72±0.13	425±14.7	247±36.8
RY174 μM	2.40±0.30	658±33.0	273±33.0	2.21±0.12	657±28.7	297±9.4
RY174 nM	2.28±0.42	453±37.0	198±16.5	2.00±0.12	507±25.0	253±34.0
RY174 pM	2.21±0.18	506±17.0	228±12.0	1.74±0.19	440±21.6	253±25.0
RB49 μM	2.14±0.15	560±29.4	261±2.9	1.91±0.22	440±16.3	230±40.8
RB49 nM	2.62±0.074	773±20.5	295±10.8	2.15±0.31	610±14.1	283±28.7
RB49 pM	2.37±0.12	690±24.4	290±24.8	2.29±0.27	610±32.7	267±12.5
Clean GaOOH	1.76±0.12	1213±69.0	688±8.5	1.76±0.12	1213±69.0	688±8.5

Table 3.2 Summary of the Deconvoluted C 1s XPS Data.

	In-Situ Samples Relative Concentration %					Ex-Situ Samples Relative Concentration %			
	sp2	C-C	C-O	C=O		sp2	C-C	C-O	C=O
RR198 μ M	19.27	46.25	26.24	8.23		18.66	42.18	30.58	8.58
RR198 nM	21.16	30.24	36.01	12.59		16.85	48.11	24.22	10.82
RR198 pM	27.27	33.34	29.6	9.79		19.71	42.11	27.8	10.38
RB19 μ M	11.36	60.1	16.7	11.84		12.66	54.7	21.46	11.18
RB19 nM	11.84	60.15	19.02	9		9.47	55.45	22.88	12.2
RB19 pM	11.26	59.27	18.01	11.46		9.11	55.11	23.95	11.83
RY174 μ M	19.13	47.61	21.74	11.53		17.16	54.25	16.01	12.57
RY174 nM	18.51	43.46	25.62	12.41		19.72	49.89	18.3	12.09
RY174 pM	24.26	37.62	27.02	11.1		25.84	41.92	19.74	12.5
RB49 μ M	15.81	44.63	26.56	13.01		12.96	37.87	37.64	11.53
RB49 nM	22.07	50.27	16.3	11.36		15	58.09	17.37	9.54
RB49 pM	15.6	42.92	29.76	11.71		14.04	49.76	25.51	10.68
Clean GaOOH	0	62.29	28.31	9.4		0	62.29	28.31	9.4

Table 3.3 Summary of the Deconvoluted O 1s XPS Data.

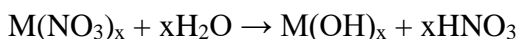
	In-Situ Samples Relative Concentration %					Ex-Situ Samples Relative Concentration %			
	O-Ga	O-C	O=C	OH		O-Ga	O-C	O=C	OH
RR198 μ M	47.96	39.19	10.72	2.12		22.3	33.7	43.6	0.41
RR198 nM	10.94	40.42	43.32	5.32		23.4	42.01	34.41	0.18
RR198 pM	25.29	54.39	19.97	0.36		20.65	43.14	35.96	0.24
RB19 μ M	23.61	49.92	26.35	0.12		19.11	66.2	14.5	0.18
RB19 nM	31.81	55.66	12.31	0.22		13.77	42.14	41.91	2.18
RB19 pM	23.72	49.47	26.49	0.33		19.36	48.9	31.61	0.13
RY174 μ M	26.9	47.76	24.87	0.47		22.98	50.43	25.76	0.82
RY174 nM	14.66	57.06	25.11	3.17		20.71	47.31	31.6	0.39
RY174 pM	18.87	61.3	19.29	0.55		27.34	43.47	27.34	1.85
RB49 μ M	24.16	43.07	31.94	0.83		22.21	48.78	28.59	0.42
RB49 nM	29.43	45.07	25.25	0.24		26.13	55.03	18.84	0
RB49 pM	24.81	38.15	36.88	0.17		22.93	32.47	44.6	0
Clean GaOOH	28.05	41.46	30.49	0		28.05	41.46	30.49	0

CHAPTER 4

Synthesis of Mixed Ga Based Oxides in the Presence of Water-Soluble Adsorbates

4.1 Introduction

In recent years, synthesis of nanostructured Ga containing materials has unlocked new and interesting applications.¹¹² The properties of GaOOH and Ga₂O₃ make them useful for catalysts, medical imaging, thermal photodynamic therapy, environmental remediation, and sensors.¹¹³ Synthesis of these materials include hydrothermal treatment, ultrasonic assisted fabrication and, sol-gel processes with the Ga being supplied by metal nitrate salts via the following reactions:¹¹⁴



Heat can be applied via a microwave approach or autoclave if the hydrothermal reaction requires temperatures above 100 °C, however many intriguing morphologies can be obtained at sub-boiling conditions. The morphology of the Ga nanostructures can be modified with surfactants during the reaction, but this is less of a green approach and reduces the potential for larger industrial applications.¹¹⁵ Sol-gel processes utilize a polymerization reaction to control particle morphology with size being controlled by the rate of the reaction. However, additional heating steps are required to remove the solvents via calcination making this method less attractive for large scale needs. Ultrasound processing can be used generate bubbles in the reaction solution via cavitation to provide localized zones of extremely high temperature and pressure upon bubble collapse. Some models of ultrasonic cavitation even suggest that light can be generated at the moment of collapse.¹⁰⁹

While pure Ga nanostructures have a wealth of applications, mixed Ga containing oxides provide additional utility by offering increased photocatalytic activity.¹¹⁶ Due to the complex

interface interactions, these nanocomposites can have a wide array of unique and specialized behaviors. $\text{Ga}_2\text{O}_3:\text{TiO}_2$ nanocomposites have been investigated for decomposition of herbicides, carburized Ga_2O_3 nanoparticles have been shown to inhibit aggregation in lithium ion batteries, and hollow Ga nanostructures exhibit persistent photoluminescent afterglow due to the internal interface. Sol-Gel processing produces alloyed (homogenous) nanoparticles and the composition can be tailored by simply changing the ratio of precursor used. Oxidation and carburization processes rely on heat treatment steps that can alter particle morphology, however such methods allow for the creation of highly tunable surface layers and morphologies.¹¹⁴

Alloys and composites are not the only way to obtain interesting interfaces.¹¹⁷ Chemical functionalization can be utilized to tune surface chemistry of Ga nanoparticles, provide unique chemical or optical signatures, modify morphology during synthesis, and stabilize particle longevity/morphology in solution. Recent studies have shown that the presence of certain ligands during precipitation can preferentially passivate crystal faces, only allowing growth along restricted axes.³¹ The presence of -OH groups on the surface of $\text{GaOOH}/\text{Ga}_2\text{O}_3$ nanostructures provides a route for simple, scalable functionalization procedures. Thus, in this work we aim to explore the synthesis of mixed Ga based oxides in the presence of water-soluble adsorbates and characterize the changes in optical properties of the different particle compositions.

4.2 Experimental

Materials Synthesis: The core materials were made via a large batch process. The clean GaOOH core synthesis follows a procedure that we have previously published. 10 g of $\text{Ga}(\text{NO}_3)_3$ was added to 400 ml DI water and the pH was raised with NaOH to a value of 8. A white precipitate formed and was washed and centrifuged with DI water three times. The clean aluminum core synthesis proceeded in much the same manner. 12.5g $\text{Al}(\text{NO}_3)_3$ was dissolved in 500 ml DI water

and the pH was raised with NaOH to a value of 8. The white precipitate was centrifuged and washed three times with DI water. The *in-situ* GaOOH core material was synthesized in 5 mM Reactive Red 198 solution instead of DI water. 1g Ga(NO₃)₃ was used for each 40 ml of solution and the pH was raised to 8 via dropwise addition of NaOH. *In-Situ* aluminum hydroxide core material was synthesized in the same manner. A 5 mM RR198 solution was prepared and 1g Al(NO₃)₃ was added per 40 ml of solution. The pH was then raised to 8 via dropwise addition of NaOH.

Layering was done by performing a precipitation reaction with nanoparticles already in solution. Approximately 1g of the core particle was diluted to 400 ml and 3g of Al(NO₃)₃ or Ga(NO₃)₃ was added to the solution. The pH was checked after addition of the salt and the particles were monitored for redissolution due to lower pH. Finally, NaOH was added to raise the pH back to 8.

Materials Characterization: All materials were characterized by SEM, XRD, FT-IR, PL. Details associated with instrumentation, experimental parameters and software used for analysis have been described by our group in the literature.^{16,118}

4.3 Results and Discussion

The Aluminum Hydroxide layered on Aluminum hydroxide (Al:Al) sample shows micron sized agglomerations of nanostructured Al(OH)₃, and the particle size distribution is very broad, Figure 4.1. GaOOH layered on Al(OH)₃ (Ga:Al) exhibits GaOOH rods ~300nm x 2um embedded in Al(OH)₃ particle agglomerations. Aluminum Hydroxide layered on *in-situ* functionalized Aluminum Hydroxide (Al:InAl) samples are 2-20+ μm irregularly shaped particles with a (wavy, textured) surface with sub-micron features. GaOOH layered on *in-situ* Al(OH)₃ (Ga:InAl) samples exhibit a wide range of particle sizes with no specific morphology emerging. EDX shows the

presence of Ga and Al atoms in the same locations, suggesting alloying has occurred. Aluminum Hydroxide layered on *ex-situ* functionalized Aluminum Hydroxide (Al:ExAl) seem to have larger individual particles than the Al:Al sample while maintaining the super-micron particle agglomeration clusters. GaOOH layered on *ex-situ* functionalized Al(OH)₃ (Ga:ExAl) particles are micron scale clusters of sub-micron particles. Unlike Ga:InAl, there are no rodlike structures present.

SEM of the GaOOH layered on GaOOH (Ga:Ga) sample shows that the particles take the form of previously reported Orzo and angular blocky structures. There does not appear to be any additional layering of GaOOH taking place, the second precipitation procedure formed new particles instead of depositing on the surface of existing GaOOH particles. Aluminum Hydroxide layered on GaOOH (Al:Ga) samples show some the GaOOH orzo particles bound together by Al(OH)₃ with the remainder of the orzo particle population remaining untethered. This is possibly due to not enough Al(NO₃)₃ precursor to form more Al(OH)₃ 'glue'. GaOOH layered on *in-situ* functionalized GaOOH (Ga:InGa) also do not show layering behavior, instead additional particles were precipitated. The GaOOH particles have a distribution of morphologies including: orzo, rhomboid, and blocky spheroid. Al(OH)₃ layered on *in-situ* functionalized GaOOH (Al:InGa) show orzo structures embedded in Al(OH)₃ matrix. Some of the smaller particles look like GaOOH plates fragmented from the orzo structure. The GaOOH layered on *ex-situ* functionalized GaOOH (Ga:ExGa) image shows regular GaOOH orzo structures interspersed with sub-micron blocky spheroids. It is postulated that the smaller particles were precipitated during the layering attempt with the RR198 dye functionalization failing to cause growth of existing particles. The Al(OH)₃ layered on *ex-situ* functionalized GaOOH (Al:ExGa) image shows similar behavior to the

Ga:ExGa sample with orzo structures interspersed with smaller irregular sphere particles. There are more rhomboidal particles than the Ga:ExGa sample.

Based on all of the detailed and quantitative SEM analysis one can see a clear difference when $\text{Ga}(\text{NO}_3)_3$ is used as the precursor to form the core material. The largest difference in shape morphology was observed in the case when $\text{Al}(\text{NO}_3)_3$ was the initial precursor followed by the introduction of $\text{Ga}(\text{NO}_3)_3$ as the next starting material. When the $\text{Al}(\text{NO}_3)_3$ precursor is used the images show the presence of large agglomerates composed of smaller particles bound together.

Additional structural characterization was done to probe phase and crystallinity of the mixed metal oxides, Figure 4.2. The Ga:Ga sample has the two main peaks at $21.4315^\circ 2\theta$ and $37.2098^\circ 2\theta$, a minor ‘fingerprint’ peak at $18.0310^\circ 2\theta$, and a complex peak region between $32.5^\circ 2\theta$ and $37.5^\circ 2\theta$. There is a GaOOH peak displacement $-0.019^\circ 2\theta$. All GaOOH peaks are accounted for in the scanned region, confirming that the prepared sample is pure GaOOH. The Al:Ga sample has the two main GaOOH peaks at $21.4406^\circ 2\theta$ and $37.2018^\circ 2\theta$ with the fingerprint peak at $18.0503^\circ 2\theta$ and a phase breakdown of 65.6% Tsumgallite (GaOOH) and 34.4% Diaspore (AlOOH). In the Ga:InGa sample the main GaOOH peaks are found at $21.3757^\circ 2\theta$ and $37.1844^\circ 2\theta$ with the fingerprint peak at $18.0453^\circ 2\theta$. The peak intensity between two main peaks is switched compared to the GaOOH sample. There is a peak displacement of $-0.101^\circ 2\theta$. In the Al:InGa spectra the main GaOOH peaks are $21.3485^\circ 2\theta$ and $37.1500^\circ 2\theta$ with the fingerprint peak at $18.1455^\circ 2\theta$ (reported shift of $-0.127^\circ 2\theta$). Two additional $\text{Al}(\text{OH})_3$ peaks appear at $18.7761^\circ 2\theta$ and $20.2810^\circ 2\theta$ (reported shift of $-0.059^\circ 2\theta$). The phase breakdown of Al:InGa is 45.6% Tsumgallite and 54.4% Bayerite. For Ga:ExGa the main GaOOH peaks are $21.3829^\circ 2\theta$ and $37.1938^\circ 2\theta$, with the fingerprint peak at $18.0573^\circ 2\theta$ ($-0.019^\circ 2\theta$ displacement). In the Al:ExGa sample the main GaOOH peaks appear at

21.3455 θ and 37.1445 θ with the small peak at 18.031 θ . The phase breakdown is 58.8% Tsumgallite, 24.1% Bayerite, and 17.1% Gibbsite.

The Ga:Al sample has the main peak at 18.0806 θ with lower intensity (<50%) peaks at 18.6928 θ (28%), 19.8098 θ (48%), and 20.0211 θ (38%) with a phase breakdown of 45.5% Bayerite [α -Al(OH)₃], 22.5% Bohemite [γ -AlO(OH)], 9.5% GaOOH, with the remainder being amorphous. Its amorphousness is evidenced by the broad wavy peaks in the 12-16 θ , 28-30 θ , 37-38 θ , 46-50 θ , and 63-70 θ regions. The Al:Al sample has a main split peak at 18.5156 θ , 18.7617 θ , and a second peak at 20.3042 θ with a phase breakdown of 80% Bayerite and 20% Gibbsite. The Ga:InAl sample exhibits some broad peaks with noisy background indicating amorphous material. There are sharp GaOOH peaks at 21.4937 θ and 37.4651 θ , however several of the peaks are unidentified with the only identifiable phase being GaOOH. The Al:InAl sample exhibits a high degree of amorphousness evidenced by the large broad peaks. The only identified phase is Gibbsite, however there are several unidentified peaks. For Ga:ExAl a triple peak at 18.2171 θ , 18.4454 θ , and 18.7415 θ represents the maximum intensity (Al shift -0.137 θ). The main GaOOH peaks are at 20.1909 θ and 40.4276 θ but are shifted and of different intensity than the pure GaOOH sample (Ga shift -0.209 θ).

The *in-situ* Al(OH)₃ core samples show a high degree of amorphous behavior compared to the other samples. When the functionalization method is changed to ex-situ Al(OH)₃ core, the samples exhibit a small degree of amorphous behavior. In mixed oxide samples the GaOOH peaks have a higher scaling factor than Al(OH)₃ phases, therefore the GaOOH signal tends to drown out the other crystal spacings making phase identification difficult.

Fourier Transform Infrared Spectroscopy was performed to confirm the presence of dye structures on the nanoparticle, Figure 4.3. The Reactive Red 198 dye is hygroscopic and a weak

hydroxyl peak is expected from 3441-3405 cm^{-1} . Signatures for benzene rings and sp^3 hybridized carbon are expected and seen in the 700-800 cm^{-1} region, and 2850-2950 cm^{-1} region respectively. Many inorganic samples adsorb water and therefore exhibit signatures in the hydroxyl region, suggesting complex and varied $-\text{OH}$ environments. The $\text{Al}(\text{OH})_3$ spectrum has a unique peak at 1395 cm^{-1} that does not appear in GaOOH samples which have a unique double peak at 1017 cm^{-1} and 950 cm^{-1} . In samples that were functionalized, the fingerprint peaks for the RR198 dye are overpowered by the GaOOH or $\text{Al}(\text{OH})_3$ fingerprint peaks, making deconvolution extremely difficult. The Al:InAl is the only sample that strongly exhibits the unique $\text{Al}(\text{OH})_3$ peak around 1400 cm^{-1} , however a small inflection can be seen in all but the GaOOH , Ga:Ga, Ga:ExGa, and Ga:InGa samples. The $\text{Al}(\text{OH})_3$ signature typically gets overshadowed by the GaOOH peaks in the mixed oxide structures with GaOOH core material. The changes in signature between mixed oxide samples supports the conclusion that changes in synthesis operations effect the binding environment of the nanostructure.

PL studies were used to assess changes in the optical properties of the oxide materials, Figure 4.4. The Reactive Red 198 dye has a main peak at 294 nm that has an inflection at 327 nm and a secondary peak at 612 nm. GaOOH has a characteristic double peak at 350 nm and 385 nm. The $\text{Al}(\text{OH})_3$ sample has two main peaks at 412 nm and 299 nm. When the composition is changed to Ga:Al the 385 nm peak remains in place and the secondary peak is located at 322 nm. When the core is swapped to Al:Ga the main peak is still at 385 with the secondary peak at 325 nm. For the Ga:InGa sample the main peak is at 385 nm with a secondary peak at 344 nm. The Al:InGa sample has a main peak at 385 nm and a secondary at 341 nm. When the 'core' material is swapped to Al:InAl there is a small inflection point at 573 nm adjacent to the main peak at 436 nm and a secondary peak at 295nm.

In the PL data, the Ga:ExAl sample has a main peak at 291nm and a split secondary peak at 328 nm and 341 nm. When the layering material is changed to Al:ExGa the main peak is at 292 nm and a split peak at 337 nm and 346 nm. The intensities of the split peaks between Ga:ExAl and Al:ExAl are switched. The Ga:ExGa has a double peak at 391 nm and 353 nm which is slightly shifted from the GaOOH sample. When the layer material is switched to Al:ExGa the main peak is 350 nm and two secondary peaks at 306 nm and 387 nm. Again, the signature for the RR198 dye is difficult to detect likely due to its lower presence on the surface of the nanoparticles.

4.4 Conclusions

In this work we carried procedures to synthesize mixed Ga based oxides using an approach where the synthesis is executive in sequential steps similar to the so-called twice hydrothermal synthesis.¹¹⁹ In this approach, the hydrothermal synthesis time is divided into two separate steps. Previously, this method was used to reduce the size of ZnO components in cellulose films while preserving transparency and improving mechanical properties as well as dielectric constant. In this work we discovered that the use of the water-soluble ligand (RR 198) alone during the two-step synthesis process did not facilitate control over the particle properties. Therefore, one needs to understand what other ligands have stronger affinity and be used to stabilize the particle formation with mixed compositions.

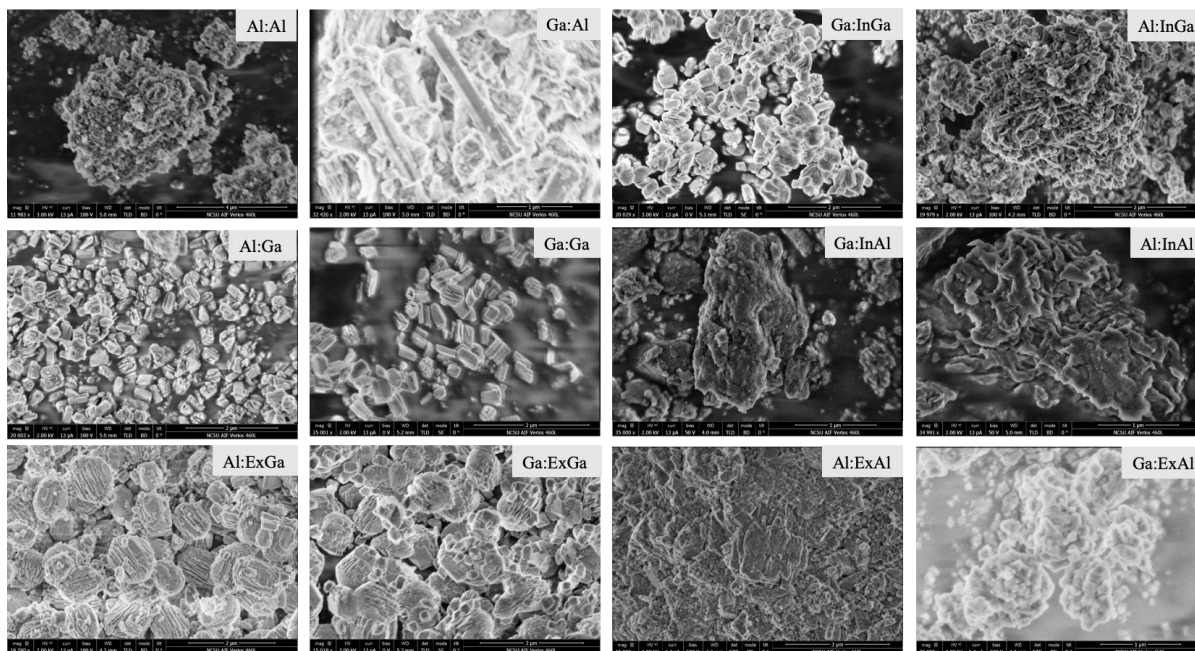


Figure 4.1 Summary of representative SEM data for each composition synthesized in this study.

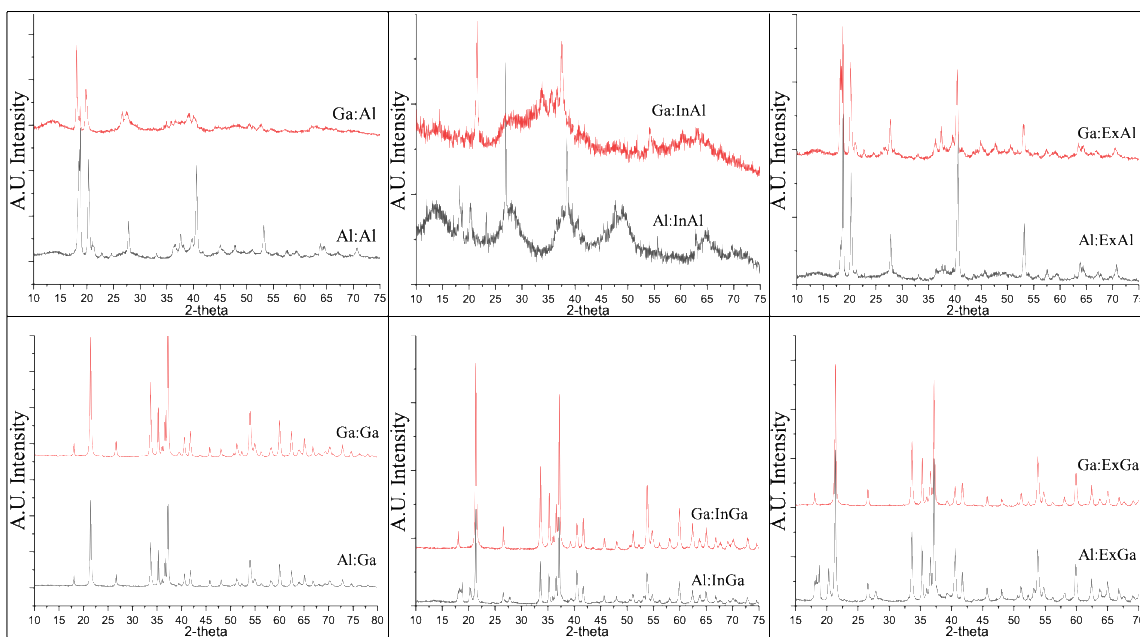


Figure 4.2 Summary of the XRD characterization performed on all of the particle compositions synthesized in this work.

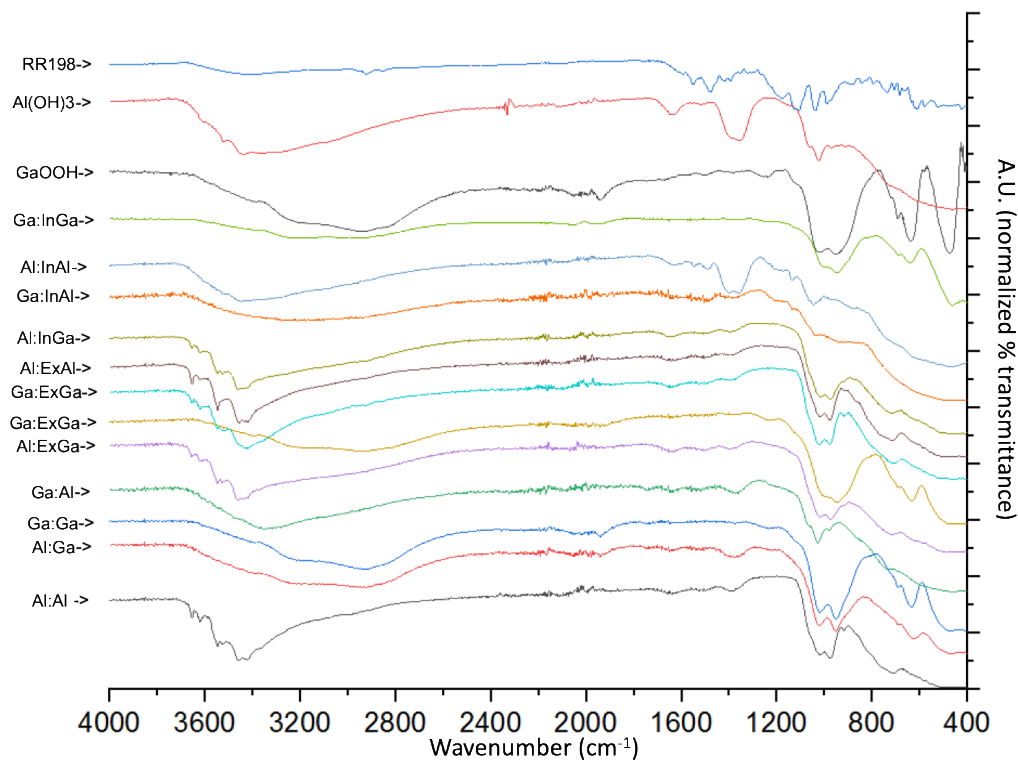


Figure 4.3 FT-IR data of the dried nanoparticles samples synthesized with different precursors and variable *in situ* (In) and *ex-situ* (Ex) conditions.

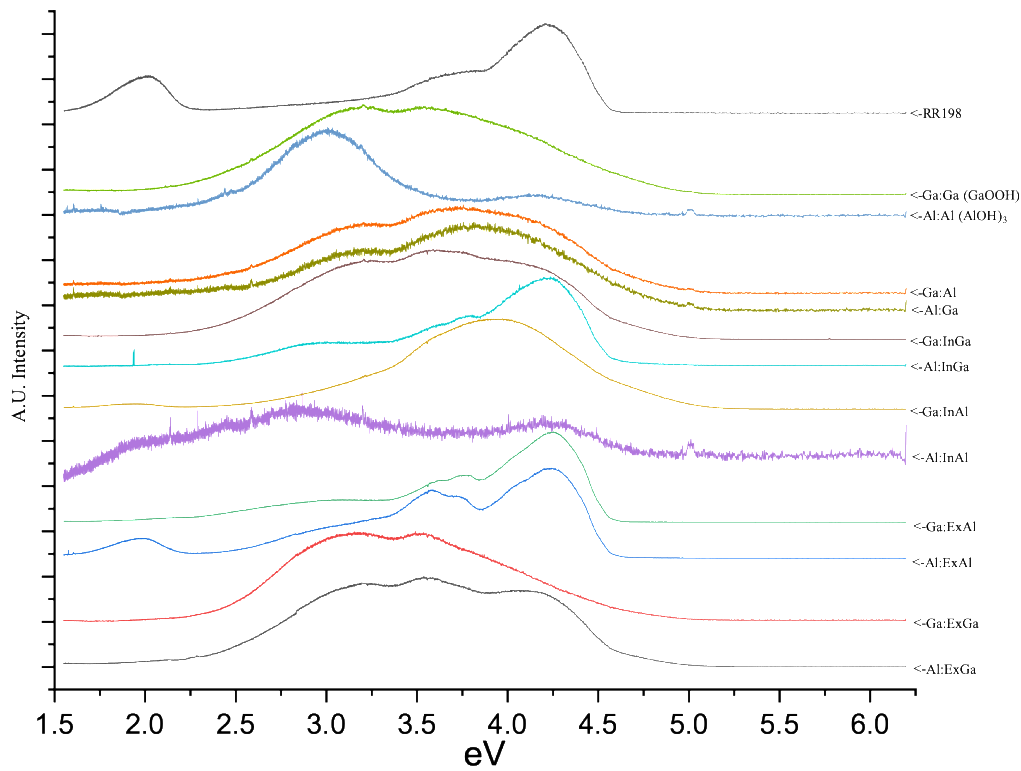


Figure 4.4 Comparison among all the PL signatures for the synthesized materials.

CHAPTER 5

Exchange reactions on GaOOH nanostructured surfaces

5.1 Introduction

Interfacial properties of planar materials can be changed via functionalization with simple ligands. The most studied example of this is thiol interaction with planar gold. Sulfur adsorbs on Au(111) forming a covalent bond that can be used as an attachment point for exchange reactions to add ligands of different length.¹²⁰ If the thiol has a ligand with strong Van der Waals forces, closely packed monolayers can be achieved.¹²¹ Other planar substrates have been investigated; they include oxides, other metals, and semiconductors. Many different methodologies have been studied to explore the strength of the functionalization bonds both in solution and gas phase. These methodologies have been adapted to a variety of configurations including nanostructured materials and colloidal materials.

Ligand bonding with nanoparticle surfaces can have a variety of important effects:¹¹⁴ surface passivation for enhanced stability,¹²² imparting novel spectroscopic properties,¹² tuned biological activity,⁹⁰ and improved self-assembly. Many different nanoparticle systems have been studied; gold, Iron Oxide and ZnS were reported by Du et al.¹²³ Early work with gold and silver citrate stabilized nanoparticles reported changes in nanoparticle stability due to changing concentrations of citrate ligand.¹²⁴ Experiments with semiconductor nanoparticles tend to focus on their photoluminescent properties, with both the core material and ligand layer effecting optical properties.¹²⁵ Other groups report increase bio-circulation of theranostically active nanoparticles due to functionalization with polypropylene glycol to mask the nanoparticle from the body.¹²⁶

Thiols are most commonly studied in relation to gold chemistry. This functional group can attach to many metal nanoparticles, but is unsuitable for iron oxide or magnetic substrates.¹²³ Some

groups report monolayers with Sulfhydryl-Terminated Alkanethiol ligands that allow for thiol-disulfide exchange reactions.¹²⁷ Thiols can only bond via monodentate coordination while sulfonic and phosphonic functional groups have 3 oxygen atoms that can participate in bonding. The multiple bonding options allow for a wider range of bonding modes/energies to be achieved. The oxygen atoms can bond to individual metal atoms at the surface, or they can form bond with the same metal site (chelation).¹²⁸ Carboxylic acid can also bind to metal oxide substrates. It exhibits a monodentate metal-ester mode or a bidentate mode attached to two metal atoms or chelating on one metal atom.

In this study we use reactive dye molecules as ligands for exchange reactions on GaOOH nanoparticles. We seek to understand the strength of the affinity of different ligands for the gallium oxyhydroxide surface. We chose the following two dyes FSS and RR198. The FSS dye is the smallest with 35 atoms a molecular weight of 376.27g, and 2 (alcohol/phenol) functional groups. Reactive Red 198 is the largest molecule with 71 atoms, a MW of 984.183g/mol, 4 sulfonic groups. We report detailed XPS analysis to understand each dyes affinity for the gallium oxyhydroxide surface.

5.2 Experimental

Dye stock solutions were prepared by weighing a small amount of dye, adding the dye to 45ml DI water, then calculating the final concentration. In the case of Reactive Red 198 2.4mg of dye was added to 45ml DI water to create a 54.2 μ m stock solution. In the case of Fluroscein Sodium Salt 6.8mg of dye was added to 45ml DI water to create a 402 μ m stock solution.

GaOOH Synthesis

The GaOOH synthesis proceeded as previously reported.²⁸ 45g of Ga(NO₃)₃ was added to 1800 ml of DI water and stirred with a stir bar until no solid remained. Under constant stirring and pH monitoring, NaOH solution was added until the pH was stable at 8. The precipitate was washed with DI water 3 times via centrifugation.

Functionalization of nanostructured GaOOH

Two dyes were used for the functionalization of GaOOH nanoparticles; Fluorescein Sodium Salt (FSS) and Reactive Red 198 (RR198). Approximately 4g of colloidal GaOOH were diluted to 800ml with DI water. The concentration of the dye solution utilized for functionalization was 1 μ m, which was prepared using the stock solutions. The particles were incubated in each dye solution for 24 hours under constant stirring. Subsequently the entire mixture was washed with DI water via centrifugation until the elute ran clear (>3x).

Exchange Reactions

The final product of the 1st functionalization reaction was portioned into 4 separate reaction vials. The first portion was centrifuged then dried in a vacuum desiccator. The other 3 portions were diluted to 200ml in separate reaction vessels for exchange reactions. Each 200ml solution was raised to 1 μ m dye concentration by addition of stock solution. Each exchange reaction was allowed to proceed for 24hrs under constant stirring. After incubation, each sample was washed via centrifugation until the elute ran clear (>3x) and dried in a low vacuum desiccation chamber.

Characterization

All samples were analyzed by XPS. Samples were prepared by pipetting a droplet of colloidal nanoparticles onto a 1 cm x 1 cm Si wafer. The wafers were then exposed to low heat

(40°C) until the water was fully driven off. XPS data was gathered using both AlK α and AgL α radiation sources to isolate the N 1s peak from the Ga auger signal.¹²⁹ The wide scans were collected using a 0.1s dwell time. AlK α high resolution spectra for each element (O 1s, C 1s, ALL) were derived by averaging 15-20 scans with a dwell time of 0.1s. AgL α high resolution spectra required 20-160 averaged scans at 0.1s dwell time. Each sample was measured once at a random spot in order to collect all the described data.

Dye reference samples were prepared in the same way on Si wafer and measured with both AlK α and AgL α radiation sources. Dye reference spectra were calibrated using C-C = 284.8 eV and spectra of functionalized nanoparticles were energy calibrated via the Ga 3d peak at 20 eV.¹³⁰ All spectra were smoothed via Savitzky–Golay linear operation with a smoothing width of 5.

For the dye reference scans the number of components used for spectral deconvolution was determined by the types of bonds observed in the pure dye. For functionalized nanoparticles, the number of components was determined by adding the components from the dye reference scan and components from the clean GaOOH scan while removing duplicates. Only Gaussian line shapes were used and every spectral region used a Shirley background.

5.3 Discussion

Unfunctionalized GaOOH nanoparticles were measured as a reference from which to make comparisons of other functionalized nanoparticles as seen in Table 5.1.¹³¹ Spectral deconvolution analysis was done on both the C 1s and O 1s data, the results of which can be seen in Figure 5.2. In the case of the O 1s environment 4 components are expected; O-Ga³⁺ at 530 eV, Ga-OH at 531.3 eV, C=O at 532.1 eV, and C-O at 533.1 eV.¹² Upon deconvolution of the data each of these species was determined to be present at the following relative abundance; 32.5 % O-Ga³⁺, 42.88 % Ga-OH, 18.6 % C=O, and 6.02 % C-O. In the case of the C 1s environment 4 components were

expected; C-C at 284.7 eV, C=O at 285.85 eV, C-O at 288.58 eV, and C=C at 283.7eV. After deconvolution of the C 1s spectra each of these species were determined to be present at the following relative abundance; 77.14 % C-C; 16.38 % C=O; 3.52 % C-O, and 2.96 % C=C. It is assumed that the presence of carbon on the clean GaOOH nanoparticles is due to environmental contamination.

Spectra were collected for both Reactive Red 198 and Fluorescein Sodium Salt dyes in pure form as a reference. Both the O 1s and C 1s spectra were collected via AlKa wavelength, and the result of the deconvolution analysis can be seen in Figure 5.2. In the case of RR198 dye, expected components are derived from the molecular structure of the dye as seen in Figure 5.1A. In the case of RR198 O 1s environment 2 components are expected; O-S at 531.9 eV and O-C at 533.6eV. Upon deconvolution of the data, both species were determined to be present at the following concentrations; 13.9 % O-C, 76.4 % O-S, and 9.7 % H₂O. In the case of the C 1s environment 6 unique carbon peaks are expected C-C at 284.6 eV, C-S at 285.2 eV, C-N at 285.6 eV, C-O at 286.2 eV, N-C-Cl at 286.1 eV, and N=C-N at 286.9eV. Upon deconvolution of the data the following species were determined to be present at the following relative abundance; 71.19 % C-C at 283.96 eV, 7.7 % C-N at 286.9 eV, 2.84 % C-O at 288.3 eV, and 18.27 % C-S at 285.24 eV. The presence of water in the O 1s environment is allowed because the RR198 dye is hygroscopic; short exposure to atmosphere can attract enough water to be detected. The large relative abundance of O-S is also expected as 14 of 15 oxygen atoms are bonded to Sulphur atoms. The two different C-N-Cl and N-C-N bonds from the structure were combined into one C-N peak.

The second dye explored was Fluorescein Sodium Salt. In the same manner as the other dye reference sample both O 1s and C 1s spectra were collected via AlKa wavelength. In the case of FSS O 1s environment 3 components are expected from the dye structure seen in Figure 5.1B;

COO at 530.9 eV, O=C at 532.4 eV, and O-C at 533.8 eV. Upon deconvolution of the data the following species were determined to be present; 52.86 % COO-, 33.44 % C-O-C, 8.97 % H₂O, and 6.72 % O=C. In the case of the C 1s environment 4 components are expected; C-C at 284.8 eV, C=C at 283.8 eV, C-O at 286.3 eV, and COO- at 288.3 eV. Upon deconvolution of the data the following species were determined to be present at the following relative abundance; 65.87 % C-C, 10.98 % C=C, 7.28 % COO-, and 15.86 % C-O. The relative distribution of components agrees with expected spectra given the FSS molecular structure. The presence of water in the O 1s spectra is accepted because the pure dye is hygroscopic and the dye was exposed to atmosphere for a short time between drying and measurement.

A portion of clean GaOOH nanoparticles were functionalized with RR198 dye. As previously stated both O 1s and C 1s spectra were collected via AlK α wavelength and the deconvolution analysis can be seen in Figure 5.3. In the case of the O 1s environment 5 unique components are expected. Ga³⁺-O at 530 eV, Ga-OH at 531.3 eV, C=O at 532.1 eV, and C-O at 533.1 eV are expected from the clean GaOOH and O-S at 531.9 eV and O-C at 533.6 eV is expected from RR198 contribution. Upon deconvolution the following species were determined to be present at the following relative abundance; 31.08 % O-Ga³⁺, 41.02 % Ga-OH, 7.24 % O=C, 3.94 % O-C, and 16.72 % O-S. Due to the presence of new material on the functionalized GaOOH nanoparticle surface, the relative abundance of components changes. For the RR198 NP O 1s environment the O-Ga³⁺, Ga-OH, O=C, and O-C components all decreased in abundance to make room for the new O-S peak as seen in Table 5.1. In the case of the C 1s environment there are 7 unique expected components; C-C at 284.7 eV, C=O at 285.85 eV, C-O at 288.58 eV, and C=C at 283.7 eV from clean GaOOH and C-C at 284.97 eV, C-N at 286.9 eV, C-O at 288.3 eV, and C-S at 285.24 eV from RR198. Upon deconvolution of the data the following species were determined

to be present at the following relative abundance; 85.64 % C-C, 3.03 % C=C, 1.05 % C-N, 5.13 % C=O, 0.39 % C-O, 2.26 % COO-, and 2.5 % C-S. Relative to clean GaOOH, the C-C, C=C, C=O and COO- components decreased in relative concentration while the C-N, C-O and C-S components increased. The relative intensities of the Clean GaOOH and the RR198 peak models were compared to give an approximation of the relative abundance of the dye on the surface of the nanoparticle. The O 1s and C 1s environments slightly disagree on the amount of signal contributions from clean GaOOH vs RR198 dye. The O 1s environment shows 80.2% contribution from GaOOH and 19.8% from RR198 dye. The C 1s environment shows 86.3% contribution from GaOOH and 13.7% from RR198 dye.

The second singly functionalized GaOOH nanoparticle is the Fluorescein Sodium salt sample. As with the other samples, both O 1s and C 1s spectra were measured via AlKa wavelength and the deconvolution analysis can be seen in Figure 5.3. In the case of the O 1s environment 5 unique components are expected O-Ga³⁺, Ga-OH, C=O, C-O, and COO-. O-Ga³⁺ at 530 eV, Ga-OH at 531.3 eV, C=O at 532.1 eV, and C-O at 533.1 eV are expected from the clean GaOOH and COO- at 530.9 eV, O=C at 532.4 eV, and O-C at 533 eV from FSS dye. Relative to clean GaOOH, O=C and O-C components decreased while O-Ga³⁺ and Ga-OH increased. In the case of the FSS NP C 1s environment the following components are expected at the listed binding energy; C-C at 284.8 eV, C=C at 283.7 eV, C-O at 286.3 eV, and COO- at 288.28 eV are from FSS dye and C-C at 284.8 eV, C=O at 285.85 eV, C-O at 288.58 eV, and C=C at 283.7eV. Upon deconvolution of the data the following species were determined to be present at the listed relative abundance; 86.76 % C-C, 3.97 % C=C, 6.03 % C=O, 0.98 % C-O, and 2.26 % COO-. Relative to clean GaOOH C-C and COO- decreased in relative abundance while C=C, C=O, and C-O increased in relative abundance. The relative intensities of the Clean GaOOH and the FSS peak models were compared

to give an approximation of the relative abundance of the dye on the surface of the nanoparticle. The O 1s and C 1s bonding environments show close agreement on the relative contribution of GaOOH vs FSS. The O 1s environment shows 95% GaOOH contribution and 5% FSS contribution while the C 1s environment shows 93.8% GaOOH contribution and 6.2% FSS contribution.

A portion of the RR198 functionalized NP were exposed to FSS in solution for 24hrs. The RR198:FSS (RR198 exchanged with FSS) functionalized GaOOH nanoparticle O 1s and C 1s regions were both measured with AlK α wavelength. In the case of the O 1s environment O-Ga³⁺, Ga-OH, O=C, O-C, O-S, and COO⁻ components are expected. O-Ga³⁺ at 530 eV, Ga-OH at 531.3 eV, C=O at 532.1 eV, and O-C at 533.1 eV are expected from clean GaOOH; COO at 530.9 eV, C=O at 532.4 eV, and O-C at 533.8 eV are expected from FSS; and O-S at 531.9 eV and O-C at 533.6 eV are expected from RR198. Upon deconvolution of the O 1s data the following components were determined to be present at the following relative abundance; 33.01 % O-Ga³⁺, 43.54% Ga-OH, 8.41% O=C, 4.22 % O-C, 8.12 % O-S, 1.67 % COO⁻, and 1.03 % H₂O. The H₂O peak was included from the dye peak models to account for potential hygroscopic effect from functionalization with dye molecules. Relative to clean GaOOH; O-Ga³⁺, Ga-OH, O-S, COO⁻, and H₂O increased in % abundance while O=C and O-C decreased in % abundance. In the case of the C 1s environment C-C, C=C, C-N, C=O, C-O, COO⁻, and C-S components are expected. C-C at 284.7 eV, C=O at 285.85 eV, C-O at 288.58 eV, and C=C at 283.7 eV from clean GaOOH; C-C at 283.96 eV, C-N at 286.9 eV, C-O at 288.3 eV, and C-S at 285.24 eV from RR198 dye; and C-C at 284.8 eV, C=C at 283.8 eV, COO⁻ at 288.2 eV, and C-O at 286.2 eV from FSS dye. Upon deconvolution the following species were determined to be present at the listed relative abundance; 87.31 % C-C, 3.84 % C=C, 0.21 % C-N, 5.91 % C=O, 0.91 % C-O, 1.31 % COO⁻, and 0.51 % C-S. The relative intensities of the Clean GaOOH, RR198, and FSS peak models were compared to

give an approximation of the relative abundance of the dye on the surface of the nanoparticle. The O 1s environment shows 86.4 % GaOOH contribution, 10.6 % RR198 contribution, and 3 % FSS contribution. The C 1s environment shows 92% GaOOH contribution, 2.8 % RR198 contribution, and 5.2 % FSS contribution.

The FSS:RR198 (FSS exchanged with RR198) functionalized GaOOH nanoparticle O 1s and C 1s regions were both measured with AlKa wavelength. In the case of the O 1s environment O-Ga³⁺, Ga-OH, O=C, O-C, O-S, and COO⁻ components are expected. O-Ga³⁺ at 530 eV, Ga-OH at 531.3 eV, C=O at 532.1 eV, and O-C at 533.1 eV are expected from clean GaOOH; COO⁻ at 530.9 eV, C=O at 532.4 eV, and O-C at 533.8 eV are expected from FSS; and O-S at 531.9 eV and O-C at 533.6 eV are expected from RR198. Upon deconvolution of the O 1s data the following components were determined to be present at the following relative abundance; 31 % O-Ga³⁺, 40.9 % Ga-OH, 10.68 % O=C, 3.86 % O-C, 13.22 % O-S, 0.05 % H₂O, and 0.29 % COO⁻. Relative to clean GaOOH; O-Ga³⁺, Ga-OH, O=C, and O-C decreased in % abundance while O-S, H₂O, and COO⁻ increased in % abundance. The H₂O peak was included from the dye peak models to account for potential hygroscopic effect from functionalization with dye molecules, however it is fit to a very small peak and could be attributed to noise depending on where the background is set. In the case of the C 1s environment C-C, C=C, C-N, C=O, C-O, COO⁻, and C-S components are expected. C-C at 284.7 eV, C=O at 285.85 eV, C-O at 288.58 eV, and C=C at 283.7 eV from clean GaOOH; C-C at 283.96 eV, C-N at 286.9 eV, C-O at 288.3 eV, and C-S at 285.24 eV from RR198 dye; and C-C at 284.8 eV, C=C at 283.8 eV, COO⁻ at 288.2 eV, and C-O at 286.2 eV from FSS dye. Upon deconvolution of the C 1s data the following species were determined to be present at the listed relative abundance; 86.5 % C-C, 3.44 % C=C, 0.48 % C-N, 5.6 % C=O, 0.5 % C-O, 2.44 % COO⁻, and 1.14 % C-S. Relative to clean GaOOH; C-C, C=C, C=O, and COO⁻ decreased in %

abundance while C-N, C-O, and C-S increased in % abundance. The relative intensities of the Clean GaOOH, RR198, and FSS peak models were compared to give an approximation of the relative abundance of the dye on the surface of the nanoparticle. The O 1s environment shows 83.8 % GaOOH contribution, 0.6 % FSS contribution, and 15.6 % RR198 contribution. The C 1s environment shows 91.8 % GaOOH contribution, 2 % FSS contribution, and 6.2 % RR198 contribution.

Table 5.1 covers the changes in each bond component relative to clean GaOOH nanoparticles. Because XPS is a surface sensitive technique, changes in relative bond expression can represent changes in the surface chemistry of the nanoparticle.¹³² In the case of the O 1s spectra, all functionalized nanoparticles that included FSS as a ligand showed increased COO- and H₂O. Similarly the RR198 functionalized nanoparticles show increased O-S relative to clean GaOOH. Both the COO- and O-S come from the unique functional group intrinsic to the respective dyes (COO- from FSS and O-S from RR198). In all cases the O=C and O-C component decreased relative to clean GaOOH. This is likely due to reduced portion of environmental contamination relative to dye contribution. In the cases where RR198 was the final functionalizing reaction, the O-Ga³⁺ and Ga-OH components decrease relative to clean GaOOH. This suggests a more substantial organic coating on the RR198 functionalized nanoparticles. In contrast, the nanoparticles functionalized with FSS last show an increase in O-Ga³⁺ and Ga-OH components, suggesting that FSS has a lower affinity to GaOOH than RR198.

In the case of the C 1s environment all samples show C-O increases and COO- decreases relative to clean GaOOH. In the cases where RR198 dye was used as a ligand (RR198, RR198:FSS, and FSS:RR198), the C-N and C-S environments both increase. In the cases of FSS NP and RR198:FSS where FSS was used as the last functionalizing ligand the C=C and C=O contributions

increased. Conversely when RR198 was the last ligand, the C=C and C=O contributions decrease. For the RR198 NP, FSS NP and FSS:RR198 NP the C-C contribution decreases and for RR198:FSS C-C increases relative to clean GaOOH.

5.4 Conclusion

The signal from the RR198 NP sample appears to be approximately 80% from the GaOOH nanoparticle and 20% from the RR198 dye at the surface. While the signal from the FSS NP appears to be approximately 95% from the GaOOH nanoparticle and 5% from the FSS dye on the surface. In addition, the RR198:FSS and FSS:RR198 samples tend to show higher relative contribution from RR198 dye vs FSS dye. This suggests that the RR198 dye has a higher affinity for GaOOH nanoparticles than FSS dye. The downward shift in expression of O-Ga³⁺ and Ga-OH when RR198 is the final ligand also suggests that the film that RR198 forms is more robust than FSS films and environmental contamination.

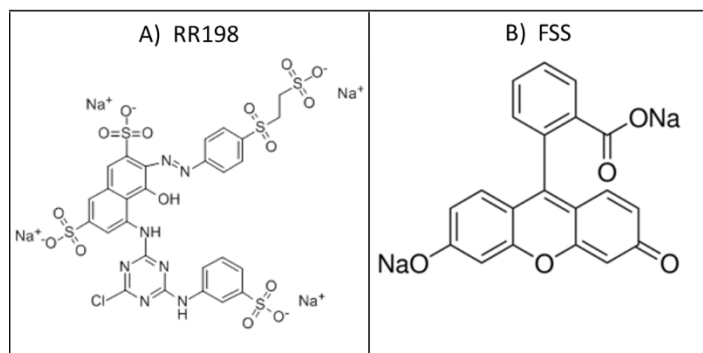


Figure 5.1 Structure of dyes used to functionalize GaOOH nanoparticles

Table 5.1 Comparison of qualitative changes of each species with respect to clean GaOOH nanoparticles

	C1s							O1s						
	C-C	C=C	C-N	C=O	C-O	COO-	C-S	O-Ga3+	Ga-OH	O=C	O-C	O-S	H2O	COO-
RR198 NP	↓	↓	↑	↓	↑	↓	↑	↓	↓	↓	↓	↑	-	-
FSS NP	↓	↑	-	↑	↑	↓	-	↑	↑	↓	↓	-	↑	↑
RR198:FSS	↑	↑	↑	↑	↑	↓	↑	↑	↑	↓	↓	↑	↑	↑
FSS:RR198	↓	↓	↑	↓	↑	↓	↑	↓	↓	↓	↓	↑	↑	↑

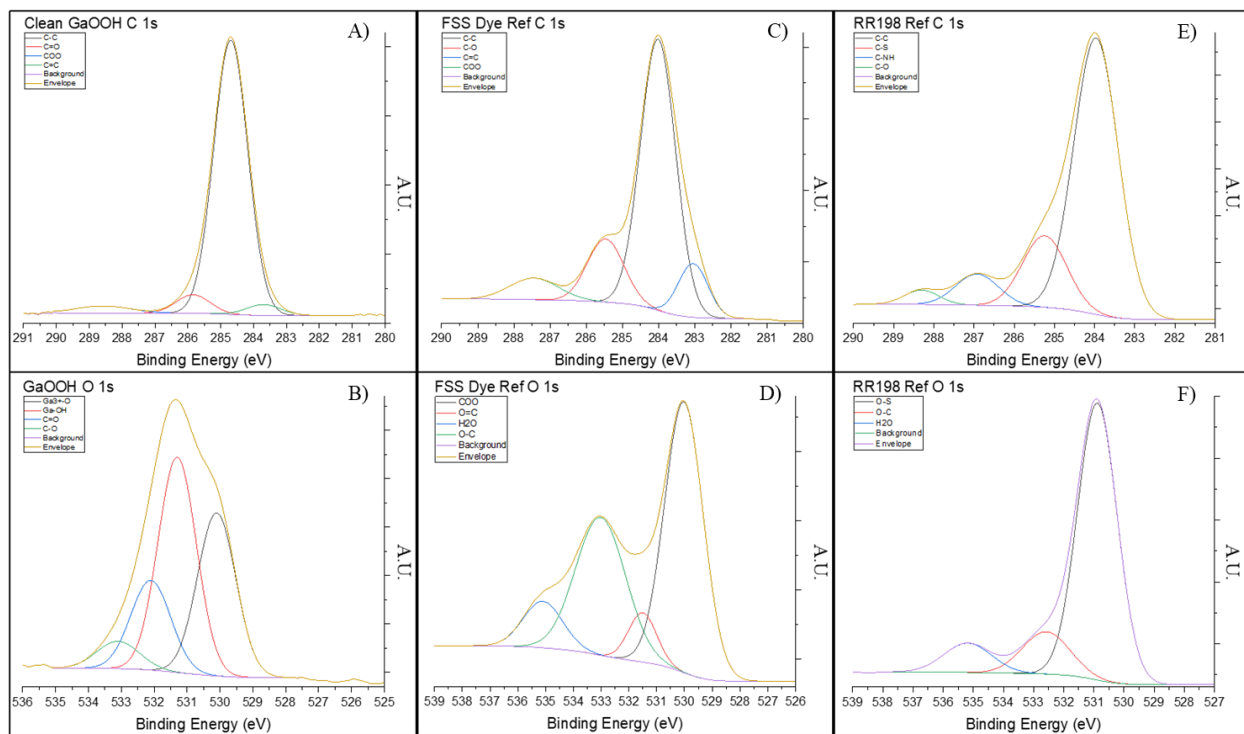


Figure 5.2 A) C 1s spectra for clean GaOOH B) O 1s XPS spectra for clean GaOOH, C) C 1s XPS spectra for FSS dye reference D) O 1s XPS spectra for FSS dye reference E) C 1s XPS spectra for RR198 dye reference F) O 1s XPS spectra for RR198 dye reference

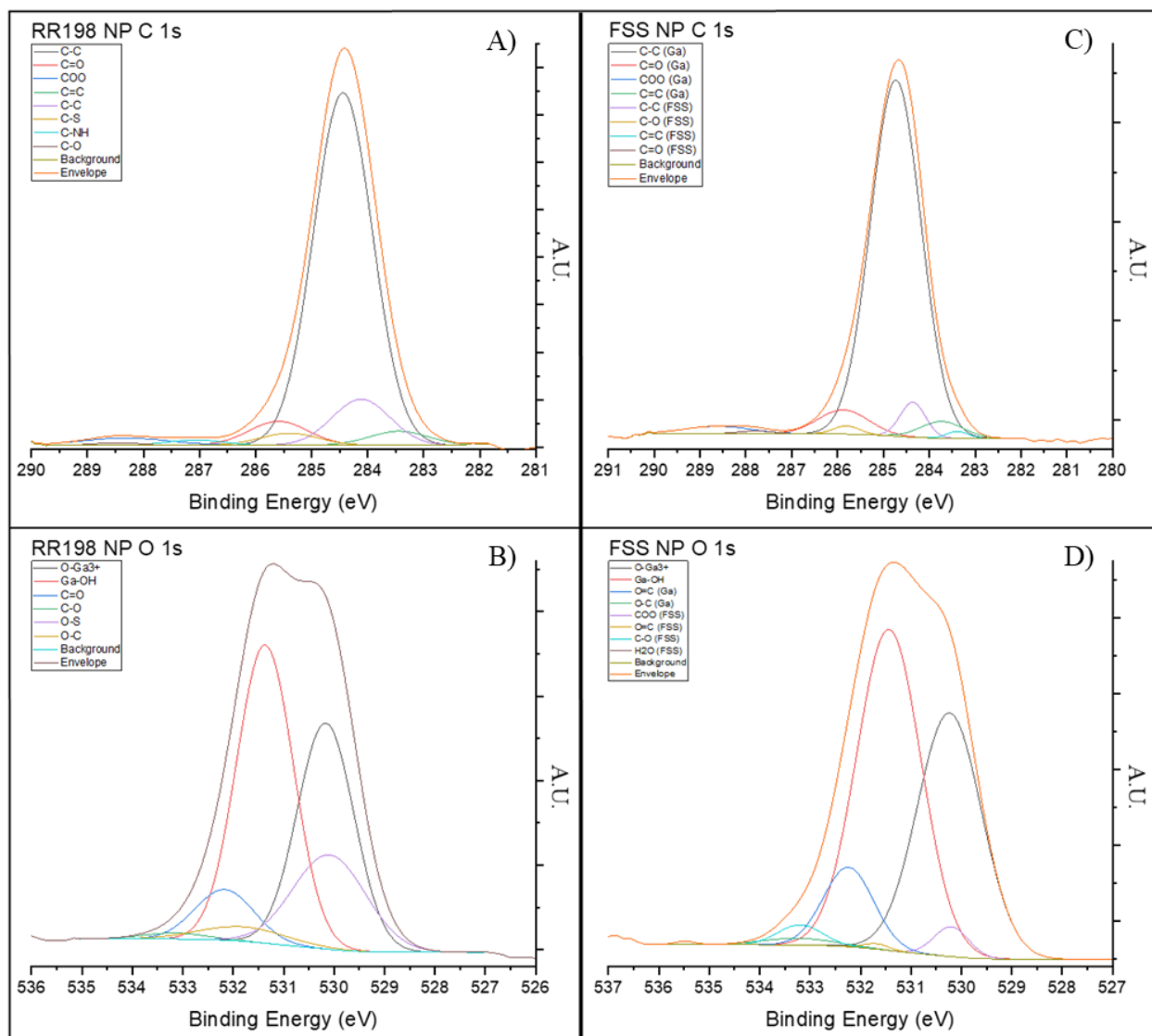


Figure 5.3 A) C 1s XPS spectra for RR198 functionalized GaOOH nanoparticles, B) O 1s XPS spectra for RR198 functionalized GaOOH nanoparticles, C) C 1s XPS spectra for FSS functionalized GaOOH nanoparticles, D) O 1s XPS spectra for FSS functionalized GaOOH nanoparticles

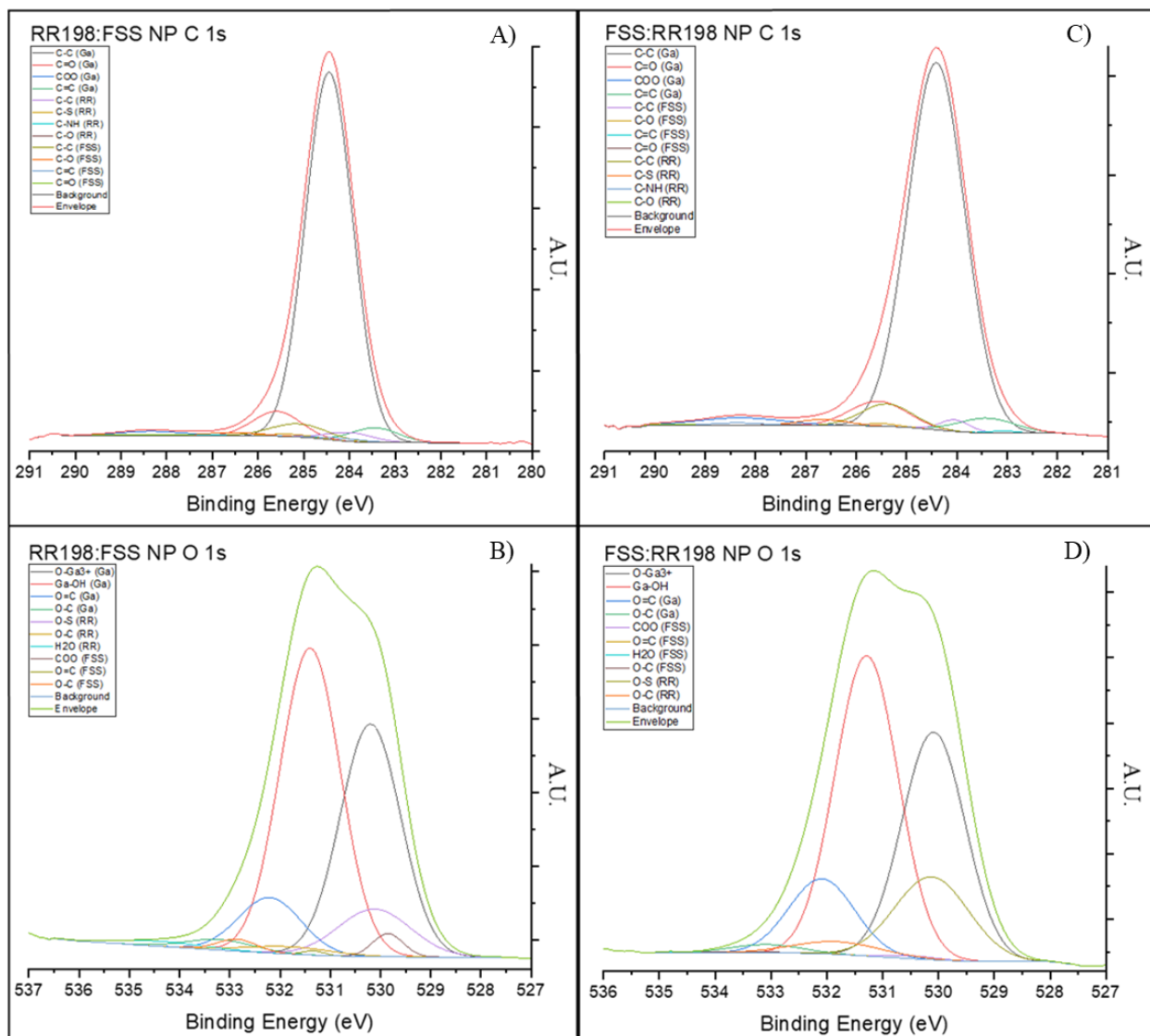


Figure 5.4 A) C 1s XPS spectra for RR198:FSS functionalized GaOOH nanoparticles, B) O 1s XPS spectra for RR198:FSS functionalized GaOOH nanoparticles, C) C 1s XPS spectra for FSS:RR198 functionalized GaOOH nanoparticles, D) O 1s XPS spectra for FSS:RR198 functionalized GaOOH nanoparticles

CHAPTER 6

Conclusions and Future Outlook

In this work we have progressed the use of GaOOH materials. Until recently, Ga based materials were used primarily in microelectronics. However, advances in fabrication of nanostructured Ga oxides have opened new avenues of research for these materials. Gallium containing oxides have favorable environmental stability, excitation and emission tunability, and photoluminescent properties. Due to their wide band gap and potential for interesting plasmonic behavior Ga based oxide materials have many possible applications from energy, to catalysis, and pre-clinical biomedical fields.¹³³ There is a need to explore how the fundamental properties of GaOOH nanoparticles change with morphology and compositional modifications. Additionally, the surface chemistry of the nanostructures can be explored to further control material properties with varying functional groups.

Initially the effect of nanoparticle morphology was studied via comparison of Orzo vs Anisotropic GaOOH nanoparticles embedded in Matrigel composites under X-ray irradiation. The wide band gap of GaOOH allows the material to catalyze the splitting of water into hydrogen and reactive oxygen species under radiation of sufficient energy.^{134,135} Upon endocytosis of the nanoparticle by a cancer cell this radiosensitization effect can be used reduce the X-ray dosage needed to achieve a given therapeutic effect. We confirmed the hypothesis that the amount of Ga³⁺ ions determines the magnitude of the ROS production. In the future, combinations of concentration and morphology can be explored to maximize the amount of free metal ions in solution.

To explore the interaction between surface chemistry and particle morphology, we designed an experiment with four reactive dyes; RR198, RB19, RB49 and RY174. The reactive dyes are water soluble and react with hydroxyl groups. We showed that GaOOH particle size and

shape can be changed via functionalization with these reactive dyes without need for high temperatures or specialized equipment. The in-situ vs ex-situ functionalization routes result in varying amounts of dye at the surface with the in-situ route providing the greatest morphological changes. Stability tests and detailed XPS analysis suggest that the dyes are not attached via functional groups, merely layered on the surface. Current efforts did not focus on controlling the layering of the dye species on the nanoparticle surface, however this interaction is ripe for future study.

We next explored mixed Gallium and Aluminum oxides. Reactive Red 198 dye was used as a functionalizing ligand in an attempt to synthesize layered nanostructures. The synthesis was performed in two sequential steps similar to the so-called twice hydrothermal synthesis. Previously, this method was used to reduce the size of ZnO components in cellulose films while preserving transparency and improving mechanical properties as well as dielectric constant.¹¹⁹ However, we discovered that the RR198 ligand alone was unsuitable as a control mechanism for particle properties as the nanostructures that formed were not layered.

Therefore, we performed further experiments by performing exchange reactions with ligands containing different functional groups to determine their relative affinity for GaOOH. Reactive Red 198 dye with sulfonic functional groups and Fluorescein Sodium Salt with a carboxylic acid functional group were used. Detailed XPS analysis was done on the C 1s and O 1s energy ranges to approximate the affinity of each dye to the GaOOH surface. A decrease in expression of O-Ga³⁺ and Ga-OH when RR198 dye is used as a ligand suggests that it forms a relatively thick layer at the surface of the NP.

Building upon the reported work in this thesis, future directions can include a number of additional experiments. Firstly, there is a wealth of untested surface chemistry with respect to

GaOOH nanostructures. There are a number of closely related adsorbate structures with sulfonic and carboxylic acid functional groups such as p-methyl red,¹³⁶ as well as dyes that rely totally on electrostatic interactions like many porphyrin derivative¹³⁷. Additionally, functionalization with varying ligands on nanoparticles of different morphologies and sizes can be applied to in vitro studies. Mixed composition Ga based nanoparticles is another largely unexplored area with potential. With the addition of a second oxide to the system band matching becomes possible, allowing for more efficient photodecomposition.^{135,138} When combined with functionalization these structures can be tested for enhanced optical or radiosensitization properties.

References

1. Pearton, S. J. *et al.* A review of Ga₂O₃ materials, processing, and devices. *Appl. Phys. Rev.* **5**, 11301 (2018).
2. Fujihara, S., Shibata, Y. & Hosono, E. Chemical deposition of rodlike GaOOH and β -Ga₂O₃ films using simple aqueous solutions. *J. Electrochem. Soc.* **152**, C764–C768 (2005).
3. Gao, L. Y., Zheng, M. J., Zhong, M., Li, M. & Ma, L. Preparation and photoinduced wettability conversion of superhydrophobic β -Ga₂O₃ nanowire film. *Appl. Phys. Lett.* **91**, 13101 (2007).
4. Kumar, V. B. *et al.* Preparation and catalytic activity of thermosensitive Ga₂O₃ nanorods. *Energy & Fuels* **30**, 7419–7427 (2016).
5. Kumar, M. *et al.* Study of GaN nanowires converted from β -Ga₂O₃ and photoconduction in a single nanowire. *Semicond. Sci. Technol.* **32**, 085012 (2017).
6. Soto, E. R. *et al.* Targeted Delivery of Glucan Particle Encapsulated Gallium Nanoparticles Inhibits HIV Growth in Human Macrophages. *J. Drug Deliv.* **2016**, 8520629 (2016).
7. Tao, J. *et al.* Investigation of growth characteristics, compositions, and properties of atomic layer deposited amorphous Zn-doped Ga₂O₃ films. *Appl. Surf. Sci.* **476**, 733–740 (2019).
8. Hirano, M., Sakoda, K. & Hirose, Y. Direct formation and phase stability of luminescent γ -Ga₂O₃ spinel nanocrystals via hydrothermal method. *J. Sol-Gel Sci. Technol.* **77**, 348–354 (2016).
9. Asakura, Y., Inaguma, Y., Ueda, K., Masubuchi, Y. & Yin, S. Synthesis of gallium oxynitride nanoparticles through hydrothermal reaction in the presence of acetylene black and their photocatalytic NO_x decomposition. *Nanoscale* **10**, 1837–1844 (2018).
10. Biegger, F. *et al.* Thioether functionalised gallium and indium alkoxides in materials

- synthesis. *New J. Chem.* **40**, 6962–6969 (2016).
11. Pearce, B. L., Berg, N. G., Jiang, L. & Ivanisevic, A. Aqueous stability of nanostructured aluminum and gallium oxyhydroxide before and after functionalization with lysine. *Mater. Lett.* **184**, 278–281 (2016).
 12. Pearce, B. L., Berg, N. G. & Ivanisevic, A. Synthesis and optical characterization of mixed nanostructured aluminum–gallium oxy-hydroxide. *Mater. Res. Lett.* **5**, 124–127 (2017).
 13. Song, L. *et al.* Low-Dose X-ray Activation of W (VI)-Doped Persistent Luminescence Nanoparticles for Deep-Tissue Photodynamic Therapy. *Adv. Funct. Mater.* **28**, 1707496 (2018).
 14. Bermudez, V. M. Functionalization of β -Ga₂O₃ Nanoribbons: A Combined Computational and Infrared Spectroscopic Study. *Langmuir* **24**, 12943–12952 (2008).
 15. Hayashi, H. & Hakuta, Y. Hydrothermal synthesis of metal oxide nanoparticles in supercritical water. *Materials (Basel)*. **3**, 3794–3817 (2010).
 16. Adams, W. T., Nolan, M. W. & Ivanisevic, A. Ga Ion-Enhanced and Particle Shape-Dependent Generation of Reactive Oxygen Species in X-ray-Irradiated Composites. *ACS Omega* **3**, 5252–5259 (2018).
 17. Xu, X. *et al.* Controlled fabrication of α -GaOOH with a novel needle-like submicron tubular structure and its enhanced photocatalytic performance. *J. Alloys Compd.* **644**, 485–490 (2015).
 18. Yang, G., Jang, S., Ren, F., Pearton, S. J. & Kim, J. Influence of High-Energy Proton Irradiation on β -Ga₂O₃ Nanobelt Field-Effect Transistors. *ACS Appl. Mater. Interfaces* **9**, 40471–40476 (2017).
 19. Yang, J. (Jeanne), Zhao, Y. & Frost, R. L. Infrared and infrared emission spectroscopy of

- gallium oxide alpha-GaO(OH) nanostructures. *Spectrochim. ACTA PART A-MOLECULAR Biomol. Spectrosc.* **74**, 398–403 (2009).
20. George, P. P. *et al.* Chemical reactions under autogenic pressure at elevated temperature to fabricate photo-luminescent Ga₂O₃ nanocrystals and their coatings. *Rsc Adv.* **1**, 619–624 (2011).
 21. Wang, J., Li, J., Yu, J., Zhang, H. & Zhang, B. Large Hollow Cavity Luminous Nanoparticles with Near-Infrared Persistent Luminescence and Tunable Sizes for Tumor Afterglow Imaging and Chemo-/Photodynamic Therapies. *ACS Nano* **12**, 4246–4258 (2018).
 22. Pearce, B. L., Berg, N. G., Rahn, M. S. & Ivanisevic, A. In situ and ex situ functionalization of nanostructured gallium oxy-hydroxide with a porphyrin dye. *Scanning* **38**, 671–683 (2016).
 23. Kollmannsberger, S. L. *et al.* Ethanol surface chemistry on MBE-grown GaN (0001), GaO_x/GaN (0001), and Ga₂O₃ (2̄ 01). *J. Chem. Phys.* **147**, 124704 (2017).
 24. Mazeina, L., Perkins, F. K., Bermudez, V. M., Arnold, S. P. & Prokes, S. M. Functionalized Ga₂O₃ Nanowires as Active Material in Room Temperature Capacitance-Based Gas Sensors. *Langmuir* **26**, 13722–13726 (2010).
 25. Wilkins, S. J., Paskova, T., Reynolds, C. L. & Ivanisevic, A. Comparison of the Stability of Functionalized GaN and GaP. *Chemphyschem* **16**, 1687–1694 (2015).
 26. Pearce, B. L., Wilkins, S. J., Paskova, T. & Ivanisevic, A. A review of in situ surface functionalization of gallium nitride via beaker wet chemistry. *J. Mater. Res.* **30**, 2859–2870 (2015).
 27. Ganguly, B. N. *et al.* Study of Gallium Oxide Nanoparticles Conjugated with β-

- Cyclodextrin: An Application To Combat Cancer. *ACS Appl. Mater. Interfaces* **8**, 17127–17137 (2016).
28. Adams IV, W. T. *et al.* Nanostructured GaOOH modified with reactive yellow, red and blue water-soluble dyes. *AIP Adv.* **9**, 25005 (2019).
 29. Cutinho, J. *et al.* Autonomous Thermal-Oxidative Composition Inversion and Texture Tuning of Liquid Metal Surfaces. *ACS Nano* **12**, 4744–4753 (2018).
 30. Farrell, Z. J. & Tabor, C. Control of Gallium Oxide Growth on Liquid Metal Eutectic Gallium/Indium Nanoparticles via Thiolation. *Langmuir* **34**, 234–240 (2018).
 31. Lin, Y., Liu, Y., Genzer, J. & Dickey, M. D. Shape-transformable liquid metal nanoparticles in aqueous solution. *Chem. Sci.* **8**, 3832–3837 (2017).
 32. Sudo, S., Kokado, K. & Sada, K. Quantum size effect and catalytic activity of nanosized single-crystalline spherical β -Ga₂O₃ particles by thermal annealing of liquid metal nanoparticles. *RSC Adv.* **7**, 678–683 (2017).
 33. Ismail, A. A., Abdelfattah, I., Faisal, M. & Helal, A. Efficient photodecomposition of herbicide imazapyr over mesoporous Ga₂O₃-TiO₂ nanocomposites. *J. Hazard. Mater.* **342**, 519–526 (2018).
 34. Tang, X. *et al.* High-Performance Ga₂O₃ Anode for Lithium-Ion Batteries. *ACS Appl. Mater. Interfaces* **10**, 5519–5526 (2018).
 35. Sánchez, J., Cortés-Hernández, D. A., Escobedo-Bocardo, J. C., Jasso-Terán, R. A. & Zugasti-Cruz, A. Bioactive magnetic nanoparticles of Fe–Ga synthesized by sol–gel for their potential use in hyperthermia treatment. *J. Mater. Sci. Mater. Med.* **25**, 2237–2242 (2014).
 36. Ristić, M., Popović, S. & Musić, S. Application of sol–gel method in the synthesis of

- gallium (III)-oxide. *Mater. Lett.* **59**, 1227–1233 (2005).
37. Sinha, G., Ganguli, D. & Chaudhuri, S. Crystallization and optical properties of finite sized β -Ga₂O₃ in sol–gel derived Ga₂O₃: SiO₂ nanocomposites. *J. Phys. Condens. Matter* **18**, 11167 (2006).
 38. Shen, W. Y., Pang, M. L., Lin, J. & Fang, J. Host-Sensitized Luminescence of Dy³⁺ in Nanocrystalline β Ga₂ O₃ Prepared by a Pechini-Type Sol-Gel Process. *J. Electrochem. Soc.* **152**, H25–H28 (2005).
 39. Nikolaev, V. I. *et al.* Growth and characterization of β -Ga₂O₃ crystals. *J. Cryst. Growth* **457**, 132–136 (2017).
 40. Burnett, D. L. *et al.* Investigation of some new hydro (solvo) thermal synthesis routes to nanostructured mixed-metal oxides. *J. Solid State Chem.* **214**, 30–37 (2014).
 41. Ho, H. P. *et al.* Synthesis of beta gallium oxide nano-ribbons from gallium arsenide by plasma immersion ion implantation and rapid thermal annealing. *Chem. Phys. Lett.* **382**, 573–577 (2003).
 42. Wang, H. *et al.* High-pressure behavior of β -Ga₂O₃ nanocrystals. *J. Appl. Phys.* **107**, 33520 (2010).
 43. Seshadri, H., Cheralathan, M. & Sinha, P. K. Photocatalytic performance of combustion-synthesized β and γ -Ga₂O₃ in the degradation of 1, 4-dioxane in aqueous solution. *Res. Chem. Intermed.* **39**, 991–1001 (2013).
 44. Xiao, H.-D. *et al.* Synthesis and structural properties of beta-gallium oxide particles from gallium nitride powder. *Mater. Chem. Phys.* **101**, 99–102 (2007).
 45. Gao, S., Xie, Y., Zhu, L. & Tian, X. The thermostability and reactivity of GaP nanocrystals in oxygen: From GaP nanocrystals to Ga₂O₃ nanocrystals. *Inorg. Chem.* **42**, 5442–5447

- (2003).
46. Ogi, T., Kaihatsu, Y., Iskandar, F., Tanabe, E. & Okuyama, K. Synthesis of nanocrystalline GaN from Ga₂O₃ nanoparticles derived from salt-assisted spray pyrolysis. *Adv. Powder Technol.* **20**, 29–34 (2009).
 47. Terasako, T., Kawasaki, Y. & Yagi, M. Growth and morphology control of β -Ga₂O₃ nanostructures by atmospheric-pressure CVD. *Thin Solid Films* **620**, 23–29 (2016).
 48. Hailin, M. & Yan, L. One-Step Preparation of β -Ga₂O₃ Nanomaterial and Research the Electrical Transport Properties at High Temperature. *Rare Met. Mater. Eng.* **42**, 2245–2247 (2013).
 49. Dai, L., You, L. P., Duan, X. F., Lian, W. C. & Qin, G. G. Synthesis of Ga₂O₃ chains with closely spaced knots connected by nanowires. *J. Cryst. Growth* **267**, 538–542 (2004).
 50. Yang, Z. X. & Jin, Y. S. The self-assembly of gallium oxide microribbons under the action of capillary forces. *Appl. Surf. Sci.* **253**, 3393–3396 (2007).
 51. Nucciarelli, F. *et al.* High Ultraviolet Absorption in Colloidal Gallium Nanoparticles Prepared from Thermal Evaporation. *Nanomaterials* **7**, 172 (2017).
 52. Playford, H. Y. *et al.* Characterization of Structural Disorder in γ -Ga₂O₃. *J. Phys. Chem. C* **118**, 16188–16198 (2014).
 53. Hirano, I., Imaoka, T. & Yamamoto, K. Deposition of gallium oxide nanodots prepared from metal-assembling dendrimer molecules isolated by the spacing of the nonmetal-assembling dendrimer molecules in the two-dendrimers mixture monolayer. *Polym. Adv. Technol.* **24**, 903–908 (2013).
 54. Jung, J.-Y. *et al.* Morphological and crystal structural characterization of Ga₂O₃ particles synthesized by a controlled precipitation and polymerized complex method. *Ceram. Int.* **42**,

- 2582–2588 (2016).
55. Zong, Y., Meng, X., Fujita, K. & Tanaka, K. Multi-color light emissions from mesoporous silica particles embedded with Ga₂O₃ nanocrystals. *Opt. Mater. Express* **4**, 518–524 (2014).
 56. Yamaguchi, A., Mashima, Y. & Iyoda, T. Reversible Size Control of Liquid-Metal Nanoparticles under Ultrasonication. *Angew. Chemie - Int. Ed.* **54**, 12809–12813 (2015).
 57. Sun, Y., Yang, S., Zhang, Y., Jiang, J. & Jiang, H. Co-Precipitation Synthesis of Gadolinium Aluminum Gallium Oxide (GAGG) via Different Precipitants. *IEEE Trans. Nucl. Sci.* **61**, 306–311 (2014).
 58. Huang, C.-C., Yeh, C.-S. & Ho, C.-J. Laser ablation synthesis of spindle-like gallium oxide hydroxide nanoparticles with the presence of cationic cetyltrimethylammonium bromide. *J. Phys. Chem. B* **108**, 4940–4945 (2004).
 59. Avivi, S., Mastai, Y., Hodes, G. & Gedanken, A. Sonochemical hydrolysis of Ga³⁺ ions: synthesis of scroll-like cylindrical nanoparticles of gallium oxide hydroxide. *J. Am. Chem. Soc.* **121**, 4196–4199 (1999).
 60. Xiao, H.-D. *et al.* Synthesis and properties of GaO₂H nanorods. *Mater. Lett.* **58**, 3925–3928 (2004).
 61. Dulda, A. Morphology controlled synthesis of α-GaO (OH) nanoparticles: thermal conversion to Ga₂O₃ and photocatalytic properties. *Adv. Mater. Sci. Eng.* **2016**, (2016).
 62. Zhao, Y., Frost, R. L., Yang, J. & Martens, W. N. Size and morphology control of gallium oxide hydroxide GaO(OH), nano- to micro-sized particles by soft-chemistry route without surfactant. *J. Phys. Chem. C* **112**, 3568–3579 (2008).
 63. Wang, X. X. *et al.* Study of the Phase Transformation of Single Particles of Ga₂O₃ by UV-

- Raman Spectroscopy and High-Resolution TEM. *Chem. Asian J.* **8**, 2189–2195 (2013).
64. Sun, M. *et al.* Rapid microwave hydrothermal synthesis of GaOOH nanorods with photocatalytic activity toward aromatic compounds. *Nanotechnology* **21**, 355601 (2010).
 65. Adeli, B. & Taghipour, F. Facile synthesis of highly efficient nano-structured gallium zinc oxynitride solid solution photocatalyst for visible-light overall water splitting. *Appl. Catal. A Gen.* **521**, 250–258 (2016).
 66. Stijepovic, I., Djenadic, R., Srdic, V. V & Winterer, M. Chemical vapour synthesis of lanthanum gallium oxide nanoparticles. *J. Eur. Ceram. Soc.* **35**, 3545–3552 (2015).
 67. Laishram, K., Mann, R. & Malhan, N. Microwave gel combustion synthesis and sinterability of Nd: GGG nanopowders. *J. Rare Earths* **32**, 521–525 (2014).
 68. Shan, J.-J., Li, C.-H., Wu, J.-M., Liu, J.-A. & Shi, Y.-S. Shape-controlled synthesis of monodispersed beta-gallium oxide crystals by a simple precipitation technique. *Ceram. Int.* **43**, 6430–6436 (2017).
 69. Wei, J., Zang, Z. & Shi, F. Synthesis, characterization and growth mechanism of β -Ga₂O₃ nano-and micrometer particles by catalyzed chemical vapor deposition. *J. Mater. Sci. Mater. Electron.* **26**, 7731–7736 (2015).
 70. Zhao, W. *et al.* Synthesis of mesoporous β -Ga₂O₃ nanorods using PEG as template: Preparation, characterization and photocatalytic properties. *J. Hazard. Mater.* **192**, 1548–1554 (2011).
 71. Qian, H.-S. *et al.* Template-free synthesis of highly uniform alpha-GaOOH spindles and conversion to alpha-Ga₂O₃ and beta-Ga₂O₃. *Cryst. Growth Des.* **8**, 1282–1287 (2008).
 72. Reddy, L. S., Ko, Y. H. & Yu, J. S. Hydrothermal Synthesis and Photocatalytic Property of β -Ga₂O₃ Nanorods. *Nanoscale Res. Lett.* **10**, 364 (2015).

73. Zhao, Y. & Frost, R. L. Raman spectroscopy and characterisation of α -gallium oxyhydroxide and β -gallium oxide nanorods. *J. Raman Spectrosc.* **39**, 1494–1501 (2008).
74. Khaing Oo, M. K. *et al.* Gold nanoparticle-enhanced and size-dependent generation of reactive oxygen species from protoporphyrin IX. *ACS Nano* **6**, 1939–1947 (2012).
75. Wyrwoll, A. J. *et al.* Size matters – The phototoxicity of TiO₂ nanomaterials. *Environ. Pollut.* **208**, 859–867 (2016).
76. Cardillo, D. *et al.* Synthesis-Dependent Surface Defects and Morphology of Hematite Nanoparticles and Their Effect on Cytotoxicity in Vitro. *ACS Appl. Mater. Interfaces* **8**, 5867–5876 (2016).
77. Schaeublin, N. M. *et al.* Does shape matter? Bioeffects of gold nanomaterials in a human skin cell model. *Langmuir* **28**, 3248–3258 (2012).
78. Laha, D. *et al.* Shape-dependent bactericidal activity of copper oxide nanoparticle mediated by DNA and membrane damage. *Elsevier Ltd* **59**, 185–191 (2014).
79. Tian, F. *et al.* Investigating the role of shape on the biological impact of gold nanoparticles in vitro. *Nanomedicine* **10**, 2643–2657 (2015).
80. Kang, S. *et al.* Comparison of cellular toxicity between multi-walled carbon nanotubes and onion-like shell-shaped carbon nanoparticles. *J. Nanoparticle Res.* **17**, 378 (2015).
81. Forest, V. *et al.* Impact of cerium oxide nanoparticles shape on their in vitro cellular toxicity. *Toxicol. Vitro.* **38**, 136–141 (2017).
82. Lee, J. H. *et al.* Rod-shaped iron oxide nanoparticles are more toxic than sphere-shaped nanoparticles to murine macrophage cells. *Environ. Toxicol. Chem.* **33**, 2759–2766 (2014).
83. Bhattacharya, D., Bhattacharyya, A. & Karmakar, P. Evaluation of Different Oxidative Stress Parameters and Apoptosis in Human Cervical Cancer Cells Exposed to Rod and

- Spherical Shaped Zinc Oxide Nanoparticles. *Bionanoscience* **6**, 1–14 (2016).
84. Kamkaew, A., Chen, F., Zhan, Y., Majewski, R. L. & Cai, W. Scintillating Nanoparticles as Energy Mediators for Enhanced Photodynamic Therapy. *ACS Nano* **10**, 3918–3935 (2016).
 85. Ronda, C., Wieczorek, H., Khanin, V. & Rodnyi, P. Review—Scintillators for Medical Imaging: A Tutorial Overview. *ECS J. Solid State Sci. Technol.* **5**, R3121–R3125 (2016).
 86. Chen, H. *et al.* Monitoring pH-triggered drug release from radioluminescent nanocapsules with X-ray excited optical luminescence. *ACS Nano* **7**, 1178–1187 (2013).
 87. Fan, W., Bu, W. & Shi, J. On the Latest Three-Stage Development of Nanomedicines based on Upconversion Nanoparticles. *Advanced Materials* **28**, 3987–4011 (2016).
 88. Retif, P. *et al.* Nanoparticles for radiation therapy enhancement: The key parameters. *Theranostics* **5**, 1030–1044 (2015).
 89. Bulin, A. L. *et al.* X-ray-induced singlet oxygen activation with nanoscintillator-coupled porphyrins. *J. Phys. Chem. C* **117**, 21583–21589 (2013).
 90. Berg, N. G. *et al.* Gallium containing composites as a tunable material to understand neuronal behavior under variable stiffness and radiation conditions. *Mater. Sci. Eng. C* **71**, 317–321 (2017).
 91. Berg, N. G. *et al.* Interfaces with Tunable Mechanical and Radiosensitizing Properties. *ACS Appl. Mater. Interfaces* **8**, 21956–21961 (2016).
 92. Chitambar, C. R. Gallium and its competing roles with iron in biological systems. *Biochimica et Biophysica Acta - Molecular Cell Research* **1863**, 2044–2053 (2016).
 93. Pribisko, M. *et al.* Cellular uptake and anticancer activity of carboxylated gallium corroles. *Proc. Natl. Acad. Sci.* **113**, E2258–E2266 (2016).

94. Schreinemachers, D. M. & Ghio, A. J. Effects of Environmental Pollutants on Cellular Iron Homeostasis and Ultimate Links to Human Disease. *Environ. Health Insights* **10**, 35–43 (2016).
95. Wu, S. *et al.* Template-free synthesis of α -GaOOH hyperbranched nanoarchitectures via crystal splitting and their optical properties. *RSC Adv.* **4**, 8209 (2014).
96. Muruganandham, M. *et al.* Solvothermal synthesis of mesoporous alpha-GaOOH semi-nanospheres. *Mater. Lett.* **111**, 137–139 (2013).
97. Muruganandham, M. *et al.* Controlled Fabrication of α -GaOOH and α -Ga₂O₃ Self-Assembly and Its Superior Photocatalytic Activity. *J. Phys. Chem. C* **116**, 44–53 (2012).
98. Koh, H. S., Yong, T., Chan, C. K. & Ramakrishna, S. Enhancement of neurite outgrowth using nano-structured scaffolds coupled with laminin. *Biomaterials* **29**, 3574–3582 (2008).
99. Betoulle, S., Etienne, J.-C. & Vernet, G. IN VIVO AND IN VITRO MODULATION OF CARP (CYPRINUS CARPIO L.) PHAGOCYTE OXIDATIVE BURST ACTIVITY BY GALLIUM. *J. Toxicol. Environ. Heal. Part A* **65**, 603–615 (2002).
100. Korystov, Y. N., Shaposhnikova, V. V, Korystova, A. F. & Emel'yanov, M. O. Detection of Reactive Oxygen Species Induced by Radiation in Cells Using the Dichlorofluorescein Assay. *Radiat. Res.* **168**, 226–232 (2007).
101. Boulton, S. *et al.* Implications of using the fluorescent probes, dihydrorhodamine 123 and 2',7'-dichlorodihydrofluorescein diacetate, for the detection of UVA-induced reactive oxygen species. *Free Radic. Res.* **45**, 139–146 (2011).
102. Snyder, P. J., Kirste, R., Collazo, R. & Ivanisevic, A. Nanoscale topography, semiconductor polarity and surface functionalization: additive and cooperative effects on PC12 cell behavior. *RSC Adv.* **6**, 97873–97881 (2016).

103. Snyder, P. J. *et al.* Noninvasive Stimulation of Neurotypic Cells Using Persistent Photoconductivity of Gallium Nitride. *ACS Omega* **3**, 615–621 (2018).
104. Berg, N. G., Nolan, M. W., Paskova, T. & Ivanisevic, A. Surface characterization of gallium nitride modified with peptides before and after exposure to ionizing radiation in solution. *Langmuir* **30**, 15477–15485 (2014).
105. Riegel, E. R., Kent, J. A. & Riegel, E. R. *Kent and Riegel's handbook of industrial chemistry and biotechnology*. (Springer, 2007).
106. Sáenz-Trevizo, A. *et al.* Chapter 2 - Functional nanostructured oxides: synthesis, properties, and applications. in *Micro and Nano Technologies* (eds. Barhoum, A. & Makhlof, A. S. H. B. T.-E. A. of N. and A. N.) 29–69 (Elsevier, 2018). doi:<https://doi.org/10.1016/B978-0-323-51254-1.00002-6>
107. Asri, R. I. M. *et al.* Corrosion and surface modification on biocompatible metals: A review. *Mater. Sci. Eng. C* **77**, 1261–1274 (2017).
108. Fang, C., Bhattarai, N., Sun, C. & Zhang, M. Functionalized Nanoparticles with Long-Term Stability in Biological Media. *Small* **5**, 1637–1641 (2009).
109. Tang, S.-Y. *et al.* Microfluidic Mass Production of Stabilized and Stealthy Liquid Metal Nanoparticles. *Small* **14**, 1800118 (2018).
110. Wilkins, S. J., Greenough, M., Arellano, C., Paskova, T. & Ivanisevic, A. In Situ Chemical Functionalization of Gallium Nitride with Phosphonic Acid Derivatives during Etching. *Langmuir* **30**, 2038–2046 (2014).
111. Wilkins, S. J., Paskova, T. & Ivanisevic, A. Modified surface chemistry, potential, and optical properties of polar gallium nitride via long chained phosphonic acids. *Appl. Surf. Sci.* **327**, 498–503 (2015).

112. Hong, S., Rhee, C. K. & Sohn, Y. Photoluminescence, electro-and thermal catalytic properties of bare and Eu (III)-doped GaOOH, α - and β -Ga₂O₃ nanorods. *J. Alloys Compd.* **774**, 11–17 (2019).
113. Huang, P. & Luan, J. Structure and photocatalytic performance of rice husk-like Ba-doped GaOOH under light irradiation. *RSC Adv.* **9**, 19930–19939 (2019).
114. Adams IV, W. T. & Ivanisevic, A. Nanostructured Oxides Containing Ga: Materials with Unique Properties for Aqueous-Based Applications. *ACS Omega* **4**, 6876–6882 (2019).
115. Das, B., Das, B., Das, N. S., Sarkar, S. & Chattopadhyay, K. K. Tailored mesoporous nanocrystalline Ga₂O₃ for dye-selective photocatalytic degradation. *Microporous Mesoporous Mater.* **288**, 109600 (2019).
116. Wang, Z., Gao, H., Niu, J., Zhang, C. & Zhang, Z. Transforming Bulk Metals into Metallic Nanostructures: A Liquid-Metal-Assisted Top-Down Dealloying Strategy with Sustainability. *ACS Sustain. Chem. Eng.* **7**, 3274–3281 (2019).
117. Akbari, M. K. *et al.* Sonochemical functionalization of the low-dimensional surface oxide of Galinstan for heterostructured optoelectronic applications. *J. Mater. Chem. C* **7**, 5584–5595 (2019).
118. Pearce, B. L., Berg, N. G. & Ivanisevic, A. Synthesis and optical characterization of mixed nanostructured aluminum–gallium oxy-hydroxide. *Mater. Res. Lett.* **5**, 124–127 (2017).
119. Ko, H.-U., Kim, H. C., Kim, J. W., Zhai, L. & Kim, J. Fabrication Method Study of ZnO Nanocoated Cellulose Film and Its Piezoelectric Property. *Materials (Basel)*. **10**, (2017).
120. Pensa, E. *et al.* The chemistry of the sulfur-gold interface: In search of a unified model. *Acc. Chem. Res.* **45**, 1183–1192 (2012).
121. Picardi, G. *et al.* Exchange of methyl- and azobenzene-terminated alkanethiols on

- polycrystalline gold studied by tip-enhanced Raman mapping. *ChemPhysChem* **15**, 276–282 (2014).
122. Merg, A. D., Zhou, Y., Smith, A. M., Millstone, J. E. & Rosi, N. L. Ligand Exchange for Controlling the Surface Chemistry and Properties of Nanoparticle Superstructures. *ChemNanoMat* **3**, 745–749 (2017).
 123. Du, L. *et al.* A Versatile Coordinating Ligand for Coating Semiconductor, Metal, and Metal Oxide Nanocrystals. *Chem. Mater.* **30**, 7269–7279 (2018).
 124. Munro, C. H., Smith, W. E., Garner, M., Clarkson, J. & White, P. C. Characterization of the Surface of a Citrate-Reduced Colloid Optimized for use as a Substrate for Surface-Enhanced Resonance Raman Scattering. *Langmuir* **11**, 3712–3720 (1995).
 125. Uematsu, T., Shimomura, E., Torimoto, T. & Kuwabata, S. Evaluation of Surface Ligands on Semiconductor Nanoparticle Surfaces Using Electron Transfer to Redox Species. *J. Phys. Chem. C* **120**, 16012–16023 (2016).
 126. Gobin, A. M., Watkins, E. M., Quevedo, E., Colvin, V. L. & West, J. L. Near-infrared-resonant gold/gold sulfide nanoparticles as a photothermal cancer therapeutic agent. *Small* **6**, 745–752 (2010).
 127. Smith, E. A. *et al.* Formation, spectroscopic characterization, and application of sulfhydryl-terminated alkanethiol monolayers for the chemical attachment of DNA onto gold surfaces. *Langmuir* **17**, 2502–2507 (2001).
 128. Monolayers, C., Pujari, S. P., Scheres, L., Marcelis, A. T. M. & Zuilhof, H. Covalent Surface Modification of Oxide Surfaces *Angewandte*. 6322–6356 (2014). doi:10.1002/anie.201306709
 129. Snyder, P. J. *et al.* Passivation of semipolar (10-1-1) GaN with different organic adsorbates.

- Mater. Lett.* **236**, 201–204 (2019).
130. Serykh, A. I. & Amiridis, M. D. In-situ X-ray photoelectron spectroscopy study of supported gallium oxide. *Surf. Sci.* **604**, 1002–1005 (2010).
 131. Pearce, B. L., Berg, N. G., Rahn, M. S. & Ivanisevic, A. In situ and ex situ functionalization of nanostructured gallium oxy-hydroxide with a porphyrin dye. *Scanning* **38**, 671–683 (2016).
 132. Hantsche, H. Comparison of basic principles of the surface-specific analytical methods: AES/SAM, ESCA (XPS), SIMS, and ISS with X-ray microanalysis, and some applications in research and industry. *Scanning* **11**, 257–280 (1989).
 133. Hou, Y., Wang, X., Wu, L., Ding, Z. & Fu, X. Efficient decomposition of benzene over a β -Ga₂O₃ photocatalyst under ambient conditions. *Environ. Sci. Technol.* **40**, 5799–5803 (2006).
 134. Shimura, K., Yoshida, T. & Yoshida, H. Photocatalytic activation of water and methane over modified gallium oxide for hydrogen production. *J. Phys. Chem. C* **114**, 11466–11474 (2010).
 135. Yanagida, T., Sakata, Y. & Imamura, H. Photocatalytic decomposition of H₂O into H₂ and O₂ over Ga₂O₃ loaded with NiO. *Chem. Lett.* **33**, 726–727 (2004).
 136. Zhang, L., Liu, X., Rao, W. & Li, J. Multilayer Dye Aggregation at Dye/TiO₂ Interface via π - π Stacking and Hydrogen Bond and Its Impact on Solar Cell Performance: A DFT Analysis. *Sci. Rep.* **6**, 1–8 (2016).
 137. Pastore, M. & Angelis, F. De. First-principles computational modeling of fluorescence resonance energy transfer in co-sensitized dye solar cells. *J. Phys. Chem. Lett.* **3**, 2146–2153 (2012).

138. Ismail, A. A., Abdelfattah, I., Faisal, M. & Helal, A. Efficient photodecomposition of herbicide imazapyr over mesoporous Ga₂O₃-TiO₂nanocomposites. *J. Hazard. Mater.* **342**, 519–526 (2018).